WAVELET NOISE REDUCTION AND VASCULAR WATER TRANSPORT MODELLING

APPLICATIONS TO DIFFUSION AND PERFUSION MRI

Bibic, Adnan

2018

Document Version:
Publisher's PDF, also known as Version of record

Link to publication

Citation for published version (APA):
Bibic, A. (2018). *WAVELET NOISE REDUCTION AND VASCULAR WATER TRANSPORT MODELLING: APPLICATIONS TO DIFFUSION AND PERFUSION MRI* (1 ed.). [Doctoral Thesis (compilation), Medical Radiation Physics, Lund]. Lund University.

Total number of authors:
1

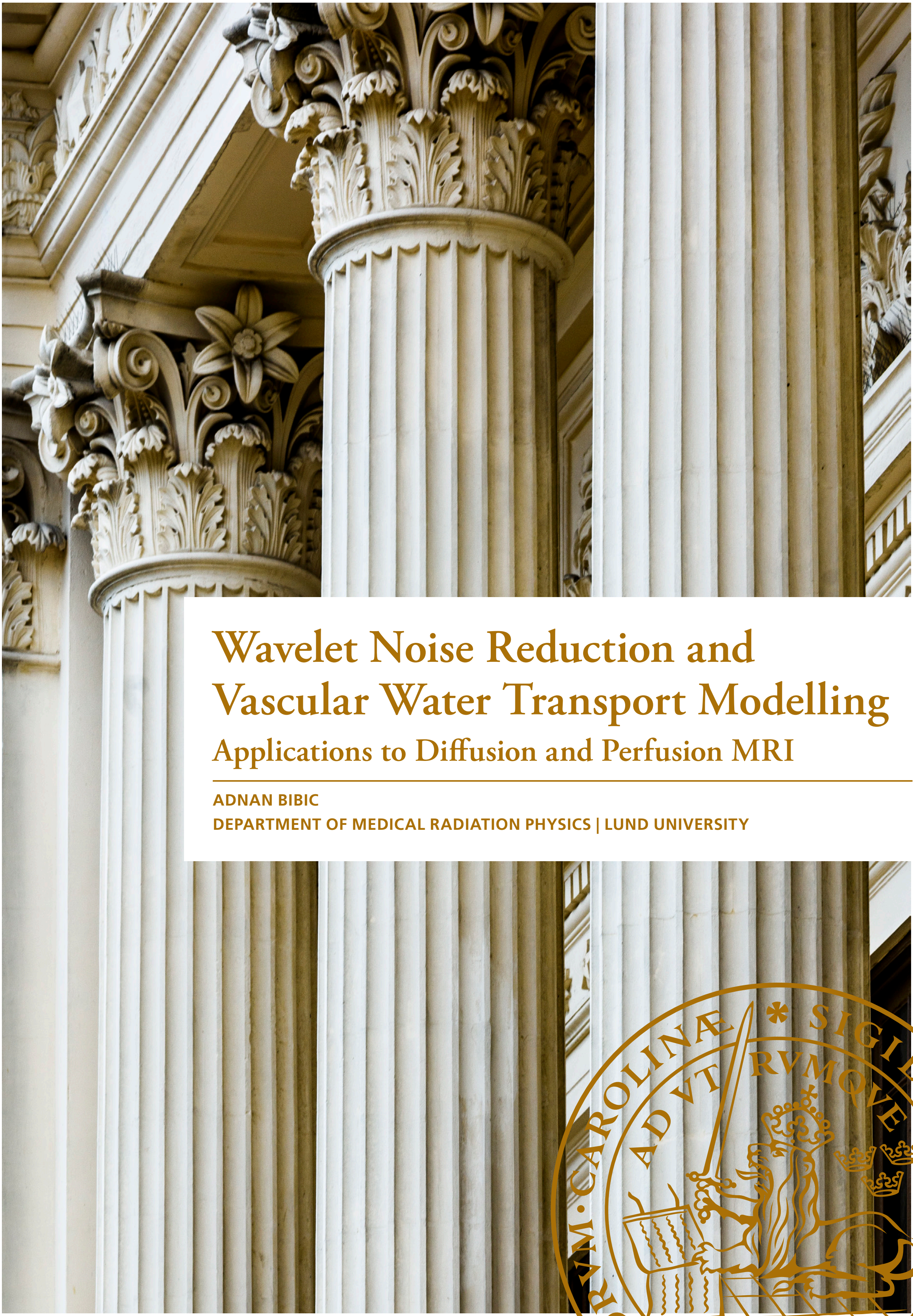

Wavelet Noise Reduction and Vascular Water Transport Modelling

Applications to Diffusion and Perfusion MRI

ADNAN BIBIC
DEPARTMENT OF MEDICAL RADIATION PHYSICS | LUND UNIVERSITY

Wavelet Noise Reduction and Vascular Water Transport Modelling

Wavelet Noise Reduction and Vascular Water Transport Modelling

Applications to Diffusion and Perfusion MRI

Adnan Bibic

LUND
UNIVERSITY

DOCTORAL THESIS
by due permission of the Faculty of Science at Lund University in Sweden.
To be publicly defended in Lecture hall F3, Centralblocket, Skåne University Hospital in Lund on Wednesday the 19th of December 2018 at 9:00 am

Faculty opponent
Professor Anders Eklund
Umeå University
Department of Radiation Sciences

Organization
LUND UNIVERSITY
Department of Medical Radiation Physics

Document name
DOCTORAL THESIS

Date of issue
23 NOVEMBER 2018

Author
ADNAN BIBIC

Sponsoring organization

Title and subtitle: WAVELET NOISE REDUCTION AND VASCULAR WATER TRANSPORT MODELLING: APPLICATIONS TO DIFFUSION AND PERFUSION MRI

Magnetic resonance imaging (MRI) is a powerful medical imaging technique, used to detect and characterise a range of diseases and conditions. It is based on the use of a strong static magnetic field in combination with magnetic field gradients and pulsed radiofrequency electromagnetic fields to visualise various organs and structures in the body according to their morphology or function.

Diffusion and perfusion MRI are established methods for quantitative measurements, often used in neurological and neurovascular clinical applications. Although these techniques are often used separately to investigate a number of diseases, combined diffusion and perfusion information can provide unique information, e.g. for assessment of whether stroke patients in the acute stage are likely to benefit from reperfusion therapy. This may be accomplished by identification of the so-called ischemic penumbra (i.e. the area surrounding the core of an infarct, exhibiting disturbed microcirculation but still viable and salvageable if the local blood supply is efficiently restored). This identification concept is often referred to as the diffusion–perfusion mismatch. In oncological applications, a combination of diffusion and perfusion MRI is sometimes used in tumour characterisation and in attempts to monitor early treatment response.

Quantitative diffusion MRI may be hampered by a bias induced by the so-called rectified noise floor in areas with low signal-to-noise ratio (SNR), and to address this issue, a wavelet-based filtering method was presented and used for noise reduction in diffusion MRI.

Perfusion images acquired by arterial spin labelling (ASL), which is the technique investigated in the present work, suffer from inherently low SNR, and this is commonly addressed by averaging multiple repetitions, which leads to a prolonged acquisition time. As an alternative approach, wavelet-domain filtering for noise reduction was applied to ASL data, and the performance of the proposed filtering technique was investigated (in terms of accuracy, precision and structural degradation), and a comparison with conventional Gaussian smoothing was also included.

Additionally, a quantitative non-compartment modelling approach for assessment of blood water transit time through the microvasculature and the blood–brain barrier (BBB) was investigated. In one study, the model was adapted to a clinical setup and applied to test–retest data from healthy volunteers, and the effects of noise on the model were examined by simulations. In an animal study, the model was further developed by introducing a bolus-tracking ASL solution that included a measured arterial input function (AIF) instead of a theoretical rectangular input function. Furthermore, it was explored whether effects of mildly damaged red blood cells on microvascular parameters were detectable using the proposed modelling approach and by ASL-based CBF quantification.

The extracted water transit time parameters can be used separately or in combination with conventional perfusion and diffusion estimates. Changes in the blood water transit time in the microvasculature may be related to alterations in capillary water permeability, and may thus be useful in the assessment of BBB integrity. Disturbed BBB permeability has been attributed to a number of disease states, and may be relevant to, for example, early diagnosis of Alzheimer's disease, inflammation, tumour grading and ischaemic stroke.

Key words: cerebral blood flow, perfusion, diffusion, arterial spin labelling, wavelets, filtering, denoising, blood-brain barrier, permeability

Classification system and/or index terms (if any)

Supplementary bibliographical information

Language
English

ISSN and key title

ISBN: 978-91-7753-890-5 (print)
ISBN: 978-91-7753-891-2 (pdf)

Recipient's notes

Number of pages: 87

Price

Security classification

I, the undersigned, being the copyright owner of the abstract of the above-mentioned dissertation, hereby grant to all reference sources permission to publish and disseminate the abstract of the above-mentioned dissertation.

Signature Adnan B.

Date 2018-11-12

Wavelet Noise Reduction and Vascular Water Transport Modelling

Applications to Diffusion and Perfusion MRI

Doctoral Thesis

Adnan Bibic

Department of Medical Radiation Physics
Lund University

2018

LUND UNIVERSITY
Faculty of Science

Main supervisor: Professor **Ronnie Wirestam**
Supervisors: Professor **Linda Knutsson** and Professor **Freddy Ståhlberg**

Cover photo: Kennet Ruona

Department of Medical Radiation Physics
Faculty of Science
Lund University
SE-221 85 Lund, Sweden

ISBN: 978-91-7753-890-5 (print)
ISSN: 978-91-7753-891-2 (pdf)

Printed in Sweden by Media-Tryck, Lund University
Lund 2018

MADE IN SWEDEN

Media-Tryck is an environmentally
certified and ISO 14001 certified
provider of printed material.
Read more about our environmental
work at www.mediatryck.lu.se

"We appeal as human beings to human beings:
Remember your humanity, and forget the rest"

MAX BORN
PERCY W. BRIDGMAN
ALBERT EINSTEIN
LEOPOLD INFELD
FREDERIC JOLIOT-CURIE
HERMAN J. MULLER
LINUS PAULING
CECIL F. POWELL
JOSEPH ROTBLAT
BERTRAND RUSSELL
HIDEKI YUKAWA

Table of contents

Abstract

Magnetic resonance imaging (MRI) is a powerful medical imaging technique, used to detect and characterise a range of diseases and conditions. It is based on the use of a strong static magnetic field in combination with magnetic field gradients and pulsed radiofrequency electromagnetic fields to visualise various organs and structures in the body according to their morphology or function.

Diffusion and perfusion MRI are established methods for quantitative measurements, often used in neurological and neurovascular clinical applications. Although these techniques are often used separately to investigate a number of diseases, combined diffusion and perfusion information can provide unique information, e.g. for assessment of whether stroke patients in the acute stage are likely to benefit from reperfusion therapy. This may be accomplished by identification of the so-called ischemic penumbra (i.e. the area surrounding the core of an infarct, exhibiting disturbed microcirculation but still viable and salvageable if the local blood supply is efficiently restored). This identification concept is often referred to as the diffusion–perfusion mismatch. In oncological applications, a combination of diffusion and perfusion MRI is sometimes used in tumour characterisation and in attempts to monitor early treatment response.

Quantitative diffusion MRI may be hampered by a bias induced by the so-called rectified noise floor in areas with low signal-to-noise ratio (SNR). Perfusion images acquired by arterial spin labelling (ASL), which is the technique investigated in the present work, suffer from inherently low SNR, and this is commonly addressed by averaging multiple repetitions, which leads to a prolonged acquisition time.

In this doctoral thesis, a wavelet-based filtering method was presented and used for noise reduction in diffusion and ASL MRI. Furthermore, the performance of the proposed filtering technique was investigated, focusing on accuracy, precision and structural degradation, and a comparison with conventional Gaussian smoothing was included for ASL images.

Additionally, a quantitative non-compartment modelling approach for assessment of blood water transit time through the microvasculature and the blood–brain barrier (BBB) was adapted to a clinical setup, and the effects of noise on the model were investigated. The model was further developed by introducing a bolus-tracking ASL solution that included a measured arterial input function (AIF) instead of a theoretical rectangular input function. Furthermore, it was explored whether effects of mildly damaged RBCs on microvascular parameters were detectable using the proposed modelling approach and by ASL-based CBF quantification. The extracted non-compartment model parameters can be used separately or in combination with conventional perfusion and diffusion estimates, and potential applications range from diagnosis to monitoring of disease progression and follow-up of therapy. Changes in the blood water transit time in the microvasculature may be related to alterations in capillary water permeability, and may thus be useful in the assessment of BBB integrity. Disturbed BBB permeability has been attributed to a number of disease states, and may be relevant to, for example, early diagnosis of Alzheimer's disease, inflammation, tumour grading and ischemic stroke.

Keywords: cerebral blood flow, perfusion, diffusion, arterial spin labelling, wavelets, filtering, denoising, blood-brain barrier, permeability

Summary in Swedish – Sammanfattning på svenska

Avbildning med hjälp av magnetresonans (MR) är en teknik som används i klinisk diagnostik för att upptäcka och karakterisera en rad sjukdomstillstånd. Metoden baseras på en kombination av statiskt magnetfält, magnetfältsgradienter och pulsade radiofrekventa elektromagnetiska fält i en magnetkamera för avbildning av form och struktur (morfologi) samt vissa funktioner hos olika organ i kroppen.

Diffusions- och perfusionsviktade MR-bilder kan tillhandahålla information utöver vad som återges i konventionella morfologiska MR-bilder. Diffusionsviktade bilder används för avbildning av vattenmolekylers termiska rörelse i vävnaden, och graden av rörelse ger information om underliggande vävnads- och cellstruktur. Tekniken kan därmed bidra till att avslöja en rad sjukdomar, t.ex. tumörer, vissa skelettsjukdomar samt sjukdomar i hjärnans blodkärl. Studier av kapillärt blodflöde (genomblödning, perfusion) är också av stor vikt för diagnostik av cerebrovaskulära sjukdomar, samt vid tumörsjukdomar där ökat blodflöde och förändrad mikrovaskulatur kan relatera till aggressivitetsgrad hos tumören. I detta avhandlingsarbete studeras en perfusionsmätningsteknik som kallas arteriell spinnmärkning (arterial spin labelling, ASL), som är en icke-invasiv MR-metodik för kvantifiering av cerebralt blodflöde. Fördelar med ASL-tekniken, liksom med diffusionsmätningarna, är bl.a. att varken joniserande strålning eller exogena kontrastmedel krävs för undersökningen. I samband med hjärninfarkter kan en kombination av de båda teknikerna bidra till att, i ett tidigt skede, upptäcka de områden i hjärnan som fortfarande kan räddas (den s.k. ischemiska penumbran) om rätt behandling sätts in i tid.

En av begränsningarna med båda de ovan nämnda teknikerna är systemets signal-till-brusförhållande (signal-to-noise ratio, SNR). Kvantifieringen av vissa diffusionsbaserade parametrar försvåras av det så kallade brusgolvet, som är ett systematiskt fel i MR bilderna i situationer där SNR är lågt. Kravet på god signal finns även i ASL-tekniken, som generellt lider av lågt signal-till-brusförhållande, och detta medför att ett stort antal medelvärderingar av signalinsamlingen ofta krävs, med relativt långa undersökningstider som följd.

I detta doktorsavhandlingsarbete presenteras en filtreringsmetod för att minska systemfelet (brusgolvet) i diffusionsviktade bilder samt för att minska antalet medelvärderingar för kvantitativa blodflödesmätningar med ASL-tekniken, inklusive analys av filtreringarnas effekter på bildkvaliteten.

Denna avhandling beskriver också en metod för mätning av vattnets passagetider i mikrovaskulaturen samt genom blod-hjärnbarriären. En anpassning av modellen till klinisk MR-utrusning presenteras, samt en ytterligare vidareutveckling av modellen som validerats i prekliniska experiment. Förhoppningen är att parametrar som beskriver vattnets transporttider, eventuellt i kombination med konventionella diffusions- och perfusionsparametrar, kan bidra till bättre förståelse för sjukdomar som påverkar blod-hjärnbarriären. Exempel på potentiella tillämpningar av intresse är Alzheimers sjukdom, inflammationer, tumörkarakterisering och stroke.

List of papers

This thesis is based on the following papers.

Paper I

R. Wirestam, **A. Bibic**, J. Lätt, S. Brockstedt, F. Ståhlberg. **Denoising of complex MRI data by wavelet-domain filtering: Application to high-b-value diffusion-weighted imaging.** *Magnetic Resonance in Medicine 56(5), 1114-1120, 2006, DOI: 10.1002/mrm.21036.*

Paper II

A. Bibic, L. Knutsson, F. Ståhlberg, R. Wirestam. **Denoising of arterial spin labeling data: wavelet-domain filtering compared with Gaussian smoothing.** *Magnetic Resonance Materials in Physics Biology and Medicine 23(3), 125-137, 2010, DOI: 10.1007/s10334-010-0209-8.*

Paper III

A. Bibic, L. Knutsson, A. Schmidt, S. Månsson, K. Abdul-Kasim, J. Åkeson, M. Gunther, F. Ståhlberg, R. Wirestam. **Measurement of vascular water transport in human subjects using time-resolved pulsed arterial spin labelling.** *NMR in Biomedicine 28(8), 1059-1068, 2015, DOI: 10.1002/nbm.3344.*

Paper IV

A. Bibic, T. Sordia, L. Knutsson, F. Ståhlberg, R. Wirestam. **Assessment of regional cerebral blood flow and vascular water transport in rats subjected to reduced red blood cell deformability using time-resolved pulsed arterial spin labelling at 9.4T.** *Manuscript.*

Preliminary reports

The following preliminary reports were presented at international meetings and conferences

I. Wirestam R., **Bibic A.**, Lätt J., Brockstedt S., Ståhlberg F. **Denoising of complex MRI data by wavelet-domain filtering: Application to high b-value diffusion weighted imaging.** *14th Scientific Meeting of the International Society for Magnetic Resonance in Medicine, Seattle, Washington, USA, May 6-12, 2006.*

II. **Bibic A.**, Knutsson L., Wirestam R., Ståhlberg F. **MR-perfusionsmätning med arteriell spinnmärkning (arterial spin labelling, ASL): Filtrering med Wiener-liknande filter i wavelet-domänen.** *Svenska Läkaresällskapets Riksstämma, Göteborg 29 November 29 – December 1, 2006.*

III. **Bibic A.**, Knutsson L., Markenroth Bloch K., Ståhlberg F., Wirestam R. **Denoising of perfusion arterial spin labeling data by wavelet-domain filtering.** *15th Scientific Meeting of the International Society for Magnetic Resonance in Medicine, Berlin, Germany, May 19-25, 2007.*

IV. **Bibic A.**, Knutsson L., Wirestam R., Mannfolk P., Olsrud J., Markenroth Bloch K., Ståhlberg F. **Wavelet-based filtering of arterial spin labeling (ASL) fMRI data using a Wiener-like filter.** *15th Scientific Meeting of the International Society for Magnetic Resonance in Medicine, Berlin, Germany, May 19-25, 2007.*

V. Knutsson L., Markenroth Bloch K., Nilsson A., **Bibic A.**, Holtås S., Wirestam R., Ståhlberg F. **Model-free arterial spin labelling CBF quantification using regional arterial input functions identified by factor analysis.** *15th Scientific Meeting of the International Society for Magnetic Resonance in Medicine, Berlin, Germany, May 19-25, 2007.*

VI. **Bibic A.**, Knutsson L., Ståhlberg F., Wirestam R. **The influence of wavelet-domain filtering and Gaussian smoothing on simulated ASL perfusion maps.** *25th Annual Meeting of the European Society for Magnetic Resonance in Medicine and Biology (ESMRMB 2008), Valencia, Spain, October 2-4, 2008.*

VII. **Bibic A.**, Knutsson L., Ståhlberg F., Wirestam R. **ASL-fMRI data analysis in the wavelet domain.** 26th Annual Meeting of the European Society for Magnetic Resonance in Medicine and Biology (ESMRMB 2009), Antalya, Turkey, October 1-3, 2009.

VIII. **Bibic A.**, Knutsson L., Ståhlberg F., Wirestam R. **Calculations of arterial transit time, total transit time and mean distribution time using pulsed time-resolved arterial spin labeling MRI.** *XXVth International Symposium on Cerebral Blood Flow, Metabolism and Function (BRAIN 2011), Barcelona, Spain, May 25-28, 2011.*

IX. **Bibic A.**, Knutsson L, Schmidt A., Månsson S., Abul-Kasim K., Åkesson J., Ståhlberg F., Wirestam R. **Calculations of arterial transit time, total transit time and mean distribution time using pulsed time-resolved arterial spin labeling MRI.** *29th Annual Scientific Meeting, ESMRMB 2012, Lisbon, Portugal, October 4-6, 2012.*

X. Madru R., Axelsson J., Tran T., **Bibic A.**, Knutsson L., Strand S.-E. **^{68}Ga-labeled superparamagnetic nanoparticles for multiple PET/MR/Cherenkov luminescence imaging of sentinel nodes.** *SNMMI Annual Meeting, Vancouver, BC, Canada, June 8-12, 2013.*

XI. **Bibic A.**, Sordia T., Henningsson E., Knutsson L., Ståhlberg F., and Wirestam R. **Quantification of vascular water transport using time-resolved pulsed arterial spin labelling MRI at 9.4 T.** *25th ISMRM Annual Meeting, Honolulu, USA, April 22-27, 2017.*

Papers not included in the thesis

I. Madru R, Tran TA, Axelsson J, Ingvar C, **Bibic A**, Ståhlberg F, Knutsson L, Strand S-E. **(68)Ga-labeled superparamagnetic iron oxide nanoparticles (SPIONs) for multi-modality PET/MR/Cherenkov luminescence imaging of sentinel lymph nodes.** Am J Nucl Med Mol Imaging. 2013;4(1):60-9. *Retrieved from http://www.ajnmmi.us*

II. Sanchez-Heredia JD, Avendal J, **Bibic A**, Lau BK. **Radiative MRI Coil Design Using Parasitic Scatterers: MRI Yagi**. IEEE Trans Antenn Propag. 2018;66(3):1570-5. ***DOI**: 10.1109/TAP.2018.2794400*

My contribution to the papers

Paper I	I proposed significant developments of the wavelet-domain filtering method, implemented mathematical methods into useful software applications, performed simulations and evaluated results. I made substantial contributions to the first draft of the manuscript and I reviewed and commented all subsequent versions.
Paper II	I took substantial part in conceptualising the idea. I made major contributions to the project design, performed simulations and evaluated results. I was the main author of the manuscript.
Paper III	I conceived major parts of the idea and the subsequent project design. I adapted the original model to our experimental conditions, contributed significantly to the experimental implementation, optimised the MRI protocol and participated in the experiments. I performed simulations, constructed software tools and analysed and evaluated the results. I was the main author of the manuscript.
Paper IV	I conceived the project design, together with Tea Sordia, PhD. I had substantial responsibility for the experimental implementation, I optimised the MRI protocol, performed the data acquisition, analysed and post-processed the experimental data and evaluated the results. I was the main author of the manuscript.

Abbreviations

3D-GRASE	3D Gradient and Spin Echo
ADC	Apparent Diffusion Coefficient
AIF	Arterial Input Function
ASL	Arterial Spin Labelling
ATT	Arterial Transit Time
BAT	Bolus Arrival Time
BBB	Blood Brain Barrier
BL	Bolus Length
CASL	Continuous Arterial Spin Labelling
CBF	Cerebral Blood Flow
CBV	Cerebral Blood Volume
CPV	Cerebral Plasma Volume
CRCV	Cerebral Red Blood Cell Volume
CSF	Cerebrospinal Fluid
DCE	Dynamic Contrast Enhanced
DKI	Diffusion Kurtosis Imaging
DSC	Dynamic Susceptibility Contrast
DTI	Diffusion Tensor Imaging
DWI	Diffusion Weighted Imaging
EC	Extravascular Compartment
EPI	Echo Planar Imaging
EPISTAR	Echo Planar Imaging and Signal Targeting with Alternating Radio Frequency
FA	Fractional Anisotropy
FAIR	Flow-sensitive Alternating Inversion Recovery
fMRI	Functional Magnetic Resonance Imaging
FT-VSI	Fourier-transform based Velocity-Selective Inversion
GE	Gradient Echo
GPU	Graphics Processing Unit
GRAPPA	Generalised Autocalibrating Partially Parallel Acquisition
IC	Intravascular Compartment
ICA	Independent Component Analysis
ICx	Insular Cortex
IVIM	Intravoxel Incoherent Motion
K_{FA}	Kurtosis Fractional Anisotropy
MAP	Mean Apparent Propagator
MR	Magnetic Resonance
MRI	Magnetic Resonance Imaging
MT	Magnetisation Transfer
MTT	Mean Transit Time
NODDI	Neurite Orientation Dispersion and Density Imaging
ns	Non-slice-selective

OP	Occipital Lobe
PASL	Pulsed Arterial Spin Labelling
pCASL	Pseudo-continuous Arterial Spin Labelling
PET	Positron Emission Tomography
PS	Permeability Surface Area Product
PWI	Perfusion Weighted Imaging
Q2TIPS	QUIPSS II with Thin-Slice TI_1 Periodic Saturation
QUIPSS	Quantitative Imaging of Perfusion using a Single Subtraction
RF	Radiofrequency
RBC	Red Blood Cell
SAR	Specific Absorption Rate
SD	Standard Deviation
SENSE	Sensitivity Encoding
SNR	Signal-to-Noise Ratio
ss	Slice-Selective
STEAM	Stimulated Echo
TE	Echo Time
TR	Repetition Time
VTF	Vascular Transport Function
VS-ASL	Velocity-Selective Arterial Spin Labelling

Chapter 1

Introduction

Over the past three decades, diffusion and perfusion magnetic resonance imaging (MRI) techniques have been increasingly used in neurological and neurovascular clinical applications. Diffusion measurements allow the visualisation of the translational thermal mobility of tissue water, revealing information about tissue microstructure, membrane permeability and, potentially, proportions of extracellular and intracellular water, whereas perfusion imaging, using endogenous or exogenous tracers, is employed to obtain information on the hemodynamic and microvascular status. There are several clinical applications in which these techniques are useful. For example, diffusion imaging is often applied to early detection and assessment of stroke, tumour characterisation and evaluation of multiple sclerosis (1), and perfusion imaging is beneficial in the identification of tissue at risk after acute stroke, evaluation of neurodegenerative conditions and tumour assessment and characterisation (2).

It was relatively early proposed that the combination of diffusion- and perfusion-based imaging techniques can contribute considerably to the diagnostic information about certain pathological conditions, and application to ischemic stroke in the acute stage appeared to be particularly promising (3). The major goal is to determine the characteristics and extent of an acute ischemic stroke and to predict the size of the final infarct so as to be able to provide optimal treatment to the patient (4). A particularly important phenomenon is the so-called perfusion–diffusion mismatch, which provides a practical measure of the tissue at risk, often referred to as the ischemic penumbra, i.e. a region with impaired microcirculation that is, nevertheless, still viable and salvageable if the local blood supply is efficiently restored (5,6). In clinical practice, this region can be identified by MRI in terms of a mismatch between the respective lesions identified by perfusion-weighted imaging (PWI) and diffusion-weighted imaging (DWI) (7). Even though DWI is accurate and superior to CT for acute ischemic stroke diagnosis, particularly within 12 h of symptom onset (8), non-contrast-enhanced CT has remained the current diagnostic standard owing to its widespread availability and its well-established capacity to exclude intracerebral haemorrhage, which is of the utmost importance before thrombolysis initiation (9,10). In PWI, the commonly mapped parameters in this context are the cerebral blood volume (CBV), the cerebral blood flow (CBF) and the mean transit time (MTT), whereas common DWI measures include fractional anisotropy (FA) and mean diffusivity (MD). In addition, the combination of DWI and PWI can be used to characterise tumours (i.e. distinguish different tumour types, assess tumour grade and attempt to determine tumour margins) (11). The addition of approaches related to transcapillary permeability (either by water or exogenous contrast agents) may provide further information, and may help to improve the determination of tumour grade (12), to distinguish different tumour types (13), and to monitor various types of cancer therapy as well as contribute to the assessment of early treatment response (14).

However, the noise in diffusion and perfusion imaging is often cited as a problem. In DWI, the low signal-to-noise ratio (SNR) conditions, occurring particularly at high degrees of diffusion encoding (i.e. high so-called b-values), are particularly problematic because the noise introduces a bias in the signal, often referred to as the rectified noise floor (15). In perfusion MRI, contrast-agent-based techniques, such as dynamic susceptibility contrast MRI (DSC-MRI) and dynamic contrast-enhanced MRI (DCE-MRI), typically include noise-sensitive operations such as deconvolution or compartment modelling (including curve fitting). In arterial spin labelling (ASL), which is addressed in this doctoral thesis, the perfusion-weighted images suffer from inherently low SNR, as further described below.

Reduction of the noise contribution is thus of considerable importance for better quantification of diffusion and perfusion parameters. In Paper I, an edge preserving, wavelet-domain filtering method was presented and evaluated. It was used to decrease the signal bias in DWI caused by the rectified noise floor. In the study reported in Paper II, wavelet denoising was applied to ASL images, and the influence of the filtering was investigated using simulations as well as human data acquired by a clinical MRI scanner. The novel wavelet-based approach was compared with conventional Gaussian smoothing, with focus on the accuracy and precision of CBF estimates and on the structural image degradation at different noise levels. Paper III describes a non-compartment model for time-resolved ASL data that is assumed to provide additional physiological information related to capillary function. The model was adapted to clinical MRI data acquisitions, and its noise sensitivity was investigated. The measured transit-time estimates were compared with numerical results from previously reported parameters of similar scope obtained using other techniques. Finally, Paper IV reports the investigation of capillary function, which is assumed to be reflected by CBF and water transport times, in rats with reduced red blood cell (RBC) deformability, as well as an improved version of the non-compartment model of water transport that allows the use of an experimental arterial input function (AIF).

Chapter 2

Basic aspects of cerebral microstructure and microcirculation

2.1 Microstructure and water diffusion

Brain tissue is a cellular organisation that can be divided into several categories according to cell density, i.e. (i) tightly packed cellular tissue, (ii) organised tissue, (iii) fibrous tissue and (iv) low-cellularity/defective cell membranes. The varying cell architectures affect the water diffusion characteristics, and the water restriction also varies in different directions, particularly in fibrous tissue, such as white matter axons, which demonstrate highly anisotropic diffusion, whereas diffusion in benign neoplasms is typically more isotropic; furthermore, diffusion is low in tightly packed epitheloid tissues.

Biological tissue can be divided into intracellular and extracellular spaces. It is presumed that water diffusion in the extracellular space (where water molecules experience relatively free diffusion) is faster than in the intracellular space (restricted diffusion) (16), and this may be due to the internal microstructure of the cells, i.e., the presence of organelles, microtubules and periplasmic spaces (17). Furthermore, the diffusivity of water molecules is restricted in areas with high cellularity owing to the reduced ratio of extracellular to intracellular compartment volume (18). This can be explored in the estimation of tumour cell proliferation, which usually correlates with increased tumour cellularity, as demonstrated in animal models (19).

2.2 Blood and microcirculation

Blood delivers oxygen and nutrients to tissue cells and transports metabolic waste products away from them. The haematocrit, i.e. the fraction of the blood that is occupied by RBCs, is approximately 45% in normal blood (in large vessels), and it strongly influences the flow properties of blood. RBCs are filled with cytoplasm and suspended in blood plasma, both behaving as incompressible Newtonian fluids in large arteries (20). However, RBCs, which are surrounded by a thin viscoelastic membrane, act in small capillaries as a non-Newtonian suspension, with a viscosity that is dependent on RBC deformability, haematocrit and flow rate. In the study reported in Paper IV, the RBC deformability was decreased to alter the blood flow dynamics within the microvasculature of the rat brain. Owing to their small number and volume, platelets do not affect viscosity, and white blood cells influence blood viscosity only if their volume fraction is abnormally elevated (21). The membrane of the RBCs shears and bends easily, and this allows the RBCs to pass through capillaries of a significantly smaller diameter than the dimensions of unstressed RBCs (with a diameter of approximately 8 µm) (22). Mechanical interaction between the RBCs and the capillary walls causes an axial drift of RBCs toward the capillary centre, a phenomenon referred to as axial migration (23), which, in turn, causes variations in flow velocity, ranging from zero at the capillary walls to a maximum close to the centre. Therefore, the average RBC velocity (v_{RBC}) is higher than the average blood velocity (v_{blood}), which leads to a reduction of RBC transit time through the capillary network. Hence, a reduction of haematocrit values in capillaries (H_c) compared to the haematocrit values in large vessels (H_L), known as the Fåhraeus effect (24), is observed, namely,

$$\frac{H_c}{H_L} = \frac{v_{blood}}{v_{RBC}} \qquad [1]$$

The microcirculation or perfusion refers to the delivery of blood to the tissue, and the most important cerebral hemodynamic parameters in this context are cerebral blood volume (CBV), cerebral blood flow (CBF) and blood mean transit time (MTT).

CBV is usually defined as the total blood volume within a local tissue element divided by the mass of the tissue element, often given in units of ml/100g. CBV is often divided into the arteriolar, capillary and venular volumes, reported to be approximately 21%, 33% and 46% of the total CBV, respectively (25). CBV may also be divided into cerebral plasma volume (CPV) and cerebral red blood cell volume (CRCV), that is,

$$CBV = CPV + CRCV \qquad [2]$$

CBF is defined as the blood volume flow supplying a local tissue element divided by the mass of the tissue element, and is measured in units of blood volume per unit mass of tissue per unit time, typically in ml/100g/min.

MTT is defined as the average time for blood to pass through the local capillary network, from the arterial to the venous side, and is measured in units of time (often in s).

According to the central volume theorem (26,27), MTT can be calculated as

$$MTT = \frac{CBV}{CBF} \qquad [3]$$

In a positron emission tomography (PET) study by Leenders et al. (28) including 34 healthy volunteers, CBF values were measured using the oxygen-15 steady-state inhalation method, considered to be the gold standard for perfusion measurements. Examples of CBF values for different cerebral regions in this study are 22.2 ± 4.9 ml/100ml/min (mean ± SD) in white matter and 54.5 ± 12.3 ml/100g/min in insular grey matter. Examples of CBV estimates from the same study based on ^{11}CO PET, were 2.7 ± 0.6 ml/100ml in white matter and 5.2 ± 1.4 ml/100ml in insular grey matter. A decrease in CBF with increasing age has been observed in several studies (28-30), but the cause of the decline has recently been challenged and attributed primarily to partial volume effects (31). Reported values of regional CBF and CBV in rats are highly heterogeneous, and considerable variability among different brain regions has also been observed (32-35); CBF estimates ranged from 40 ml/100g/min (36) to 260 ml/100g/min (37), and reported CBV values were between 0.629 ml/100 g (6.29 µl/g) (38) and 6 ml/100 g (36).

In normal brain tissue, CBF and CBV tend to be nonlinearly correlated and the relation $CBV = 0.8 \cdot CBF^{0.38}$ has been reported by Grubb et al. (39). Their data were later reanalysed by van Zijl et al. (25) using the proposed theoretical relationship $CBV = 0.5 \cdot CBF^{0.5}$. MTT can be calculated from CBF and CBV according to Equation 3, and is typically of the order of 5 s in humans.

2.3 Blood-brain barrier and transcapillary permeability

The blood brain barrier (BBB) acts as a barrier to diffusion processes, preventing the influx of most substances from the blood to the brain parenchyma, and it is essential for the normal function of the central nervous system. The BBB is present in all brain regions, except for the circumventricular organs, as an integral part of the neuroendocrine function (40). The BBB consists mainly of tightly jointed endothelial cells and partially of the basement membrane surrounding them as well as the perivascular end feet of astrocytes.

In addition to preventing unwanted substances to enter the brain parenchyma, the BBB also hinders water from equilibrating completely with brain tissue water during a single capillary transit (41). The influx of molecules across the BBB per unit time is usually referred to as the permeability coefficient *P*. However, the total capillary area where exchange occurs, i.e. the capillary surface area *S,* is difficult to estimate, and thus this transport is often described in terms of the so-called permeability-surface area product (PS). PS has the same unit as flow and is expressed in units of ml/100g/min. The estimation of the water transport through the BBB was addressed in Papers III and IV.

Chapter 3

Basic methodology

3.1 Diffusion sensitisation

Diffusion-weighted MR imaging (DWI) is a technique for measuring the thermal molecular movements of water. Water molecules are constantly in random movement driven by internal kinetic (thermal) energy, a phenomenon known as 'Brownian motion' (42). For an ideal gas, the movement depends on temperature and particle mass, and is described by the Maxwell–Boltzmann distribution law, one of the basic tenets of statistical mechanics (43). That is,

$$f(v) = 4\pi N \left(\frac{m}{2\pi k_B T}\right)^{3/2} v^2 e^{-mv^2/2kT} \tag{4}$$

Equation 4 shows the Maxwell distribution of the velocities v of N molecules of mass m contained in a gas, where T is the absolute temperature and k_B is the Boltzmann constant.

In the diffusive regime, the measurement time t is assumed to be considerably longer than the momentum relaxation time $\tau_p = m/\gamma_S$, where γ_S is the Stokes friction coefficient, and the rate of translation or the diffusion constant $D = k_B \cdot T/\gamma_S$ (in units of mm^2s^{-1}) can be calculated. It is predicted by Einstein's theory (44), which is also applied to liquids, that in the case of free diffusion, the mean square displacement $\langle[\Delta x]^2\rangle$ of a free Brownian particle in one dimension during time t is given by

$$\langle[\Delta x]^2\rangle = 2 \cdot D \cdot t \tag{5}$$

For small values of $t \ll \tau_p$, Equation 5 is no longer valid, and in this regime, inertia dominates the dynamics of the particles and the motion is ballistic. The displacement of a particle for all time scales can be described by the so-called Langevin equation (43).

In brain tissue, the thermal movement (i.e. self-diffusion) of the water is not truly random because biological tissue contains structures and complex geometries, which may limit the degree of free diffusion, sometimes more in certain directions than in others. It is thus possible to visualise different brain-tissue microstructures by studying the effects of diffusion on the MR signal and by reconstructing the preferred paths of the water movement from the observed effects of diffusion in different cell structures and along different directions. The displacement of molecules measured by MRI is proportional to the diffusion coefficient, and the resulting parameter is normally referred to as the apparent diffusion coefficient (ADC) (45).

Basic diffusion-weighted MRI pulse sequences are obtained by adding two gradient pulses of high amplitude to the pulse sequence (Figure 1), which is often referred to as the Stejskal–Tanner approach (46). The first gradient will label the spins by assigning them a position-dependent phase angle. The second gradient pulse will re-phase or refocus the stationary spins, whereas spins that have moved will obtain a resulting net phase angle at the time of the echo (TE). The individual random motions of a large population of spins result in an intravoxel phase dispersion and an associated signal loss. To a first approximation, assuming Gaussian diffusion, the degree of signal attenuation caused by diffusion is exponentially related to the magnitude of the molecular translation (i.e. the ADC) and the degree of the diffusion sensitivity of the pulse sequence (the so-called b-value) (Equations 6 and 7).

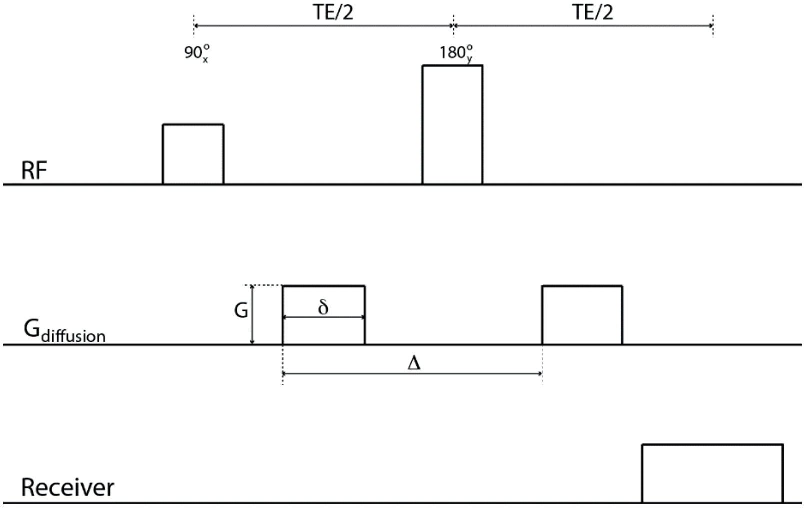

Figure 1:
Schematic illustration of a basic diffusion-sensitive spin-echo pulse sequence.

The b-value depends on the amplitude of the diffusion gradient G, the duration of each gradient pulse $\boldsymbol{\delta}$ and the time between the starting points of the two diffusion-encoding gradient pulses Δ. For rectangular diffusion gradients, b is given by

$$b = (\gamma\delta G)^2(\Delta - \delta/3) \tag{6}$$

where γ is the gyromagnetic ratio. By acquiring several images with different b-values and different gradient directions given by the unit vector $\vec{g}$, the ADC along each direction can be calculated by

$$ADC_{\vec{g}} = \frac{1}{b} ln\left(\frac{S_0}{S_g}\right) \tag{7}$$

where S_0 is the non-diffusion-weighted image intensity or signal and S_g is the diffusion-weighted signal along direction $\vec{g}$. The experiment can be conducted in different diffusion-encoding directions, and to characterise the directional dependence of diffusion, ADC can be expressed in tensor form. By calculating an ADC map for each direction, an ADC vector can be constructed (Equation 8). A minimum of six directions is necessary to completely describe the 3 × 3 diffusion tensor matrix, and the commonly used gradient scheme is

$$\left(G_x, G_y, G_z\right) = \{(1,1,0), (1,0,1), (0,1,1), (-1,1,0), (-1,0,1), (0,-1,1)\}$$

resulting in

$$ADC = M^{-1}\begin{bmatrix} ADC_{110} \\ ADC_{101} \\ ADC_{011} \\ ADC_{-110} \\ ADC_{-101} \\ ADC_{0-10} \end{bmatrix} = \begin{bmatrix} ADC_{xx} & ADC_{xy} & ADC_{xz} \\ ADC_{yx} & ADC_{yy} & ADC_{yz} \\ ADC_{zx} & ADC_{zy} & ADC_{zz} \end{bmatrix} \tag{8}$$

where *M* is a transformation matrix depending only on the applied diffusion directions. The three upper and lower off-diagonal elements in the ADC matrix are identical, i.e. $ADC_{xy} = ADC_{yx}$, $ADC_{xz} = ADC_{zx}$ and $ADC_{yz} = ADC_{zy}$. In some cases, the average diffusivity <*ADC*> is desired, and it can be calculated by averaging the diagonal elements of the diffusion tensor as follows:

$$\langle ADC \rangle = \frac{ADC_{xx} + ADC_{yy} + ADC_{zz}}{3} \quad [9]$$

Images constructed from <*ADC*> are often called trace maps. Finally, the directional variations in diffusivity can be described in terms of the fractional anisotropy (FA). This is a measure of deviation from isotropy, i.e. the degree to which the diffusion ellipsoid deviates from a sphere, and it is mathematically defined as

$$FA = \sqrt{\frac{3}{2}} \frac{\sqrt{(\lambda_1 - \bar{\lambda})^2 + (\lambda_2 - \bar{\lambda})^2 + (\lambda_3 - \bar{\lambda})^2}}{\sqrt{\lambda_1^2 + \lambda_2^2 + \lambda_3^2}} \quad [10]$$

where λ_1, λ_2 and λ_3 are the principal eigenvalues of the diffusion tensor, calculated by solving Equation 11 for λ. The left-hand side of Equation 11 represents the determinant of the tensor, i.e.

$$det \begin{bmatrix} ADC_{xx} - \lambda & ADC_{xy} & ADC_{xz} \\ ADC_{yx} & ADC_{yy} - \lambda & ADC_{yz} \\ ADC_{zx} & ADC_{zy} & ADC_{zz} - \lambda \end{bmatrix} = 0 \quad [11]$$

The mean eigenvalue is given by

$$\bar{\lambda} = \frac{\lambda_1 + \lambda_2 + \lambda_3}{3} \quad [12]$$

The use of diffusion tensors to elucidate information about tissue architecture is referred to as diffusion tensor imaging (DTI) (47). Combined with the so-called fibre tracking algorithms, DTI enables in vivo visualisation of tissue pathways (48). However, DTI can resolve only a single fibre direction within each voxel. For tissue voxels containing a distribution of fibre orientations, ADC-based methods have been shown to be inconsistent, particularly when higher b-values are used, and diffusion has been shown to be non-Gaussian (49). The non-Gaussian behaviour in DWI results in a deviation from monoexponential signal decay, and the diffusion kurtosis imaging (DKI) model has been proposed for quantifying the degree to which water diffusion differs from being Gaussian (50,51). In Paper I, deviations from the monoexponential signal decay were assumed to be described by a biexponential signal attenuation, corresponding to a two-compartment diffusion system, but in light of more recent theories, such observations are, most likely, better described by non-Gaussian diffusion models.

3.2 Arterial spin labelling methodology

ASL is a completely non-invasive MRI method for measurement of tissue perfusion, in which magnetically labelled endogenous blood water is used as a tracer. To accomplish this, the following basic strategy can be used (2): The longitudinal magnetisation of arterial blood is manipulated by inversion or saturation (i.e., 180° or 90°) radiofrequency (RF) pulses upstream to the imaging slice to make the spin magnetisation differ from the state of the static tissue, and this is referred to as blood labelling. A delay time TI is then allowed for the labelled blood to flow into the imaging slice, and during this period, the arterial magnetisation of labelled spins experiences T_1 relaxation. In the imaging slice, the labelled spins exchange completely with the tissue water, provided that water acts as a freely diffusible tracer (although it should be noted that this is not necessarily a valid assumption (41,52-54)). The magnetisation after inflow of labelled spins is measured and compared with a control image acquired in the same manner, except for blood and tissue spins being in the same magnetisation state in the control situation. In early ASL implementations, the control situation included application of an additional inversion RF pulse in a slab distal to the imaging slice to compensate for magnetisation transfer (MT) effects; however, an inversion off-resonance non-selective pulse is currently more common. The difference between the two images ideally depends only on the amount of labelled blood that entered the imaging slice and exchanged with the tissue water, and the signal difference is directly related to CBF. In Figure 2, a schematic representation of a basic ASL experiment is shown.

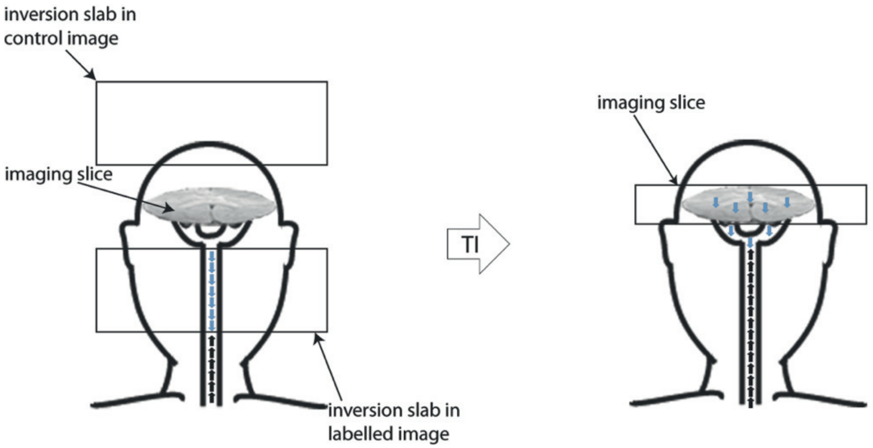

Figure 2:
Labelling principle in EPISTAR ASL. The image to the left shows the magnetisation immediately after the inversion pulse, whereas the image to the right shows the magnetisation immediately before the imaging RF pulse in the labelled image (with labelled spins in the image plane). Blue arrows represent inverted spins and black arrows represent undisturbed spins.

Various ASL techniques have been described after the introduction of the original continuous ASL (CASL) concept. CASL is based on a train of saturation pulses continuously applied to label water in the inflowing blood (55), and inversion RF pulses were later introduced to double the signal difference between control and labelling (56). The accuracy of CBF quantification was subsequently improved by minimising the MT effects by introducing an additional transmit coil (57) as a labelling coil. Pulsed ASL (PASL) approaches have also been proposed, where short inversion pulses are applied in thick slabs proximal and distal to the imaging region for the label and control experiment, respectively (cf. Figure 2), to create equal MT effects and to minimise the specific absorption rate (SAR) compared with CASL. The first PASL technique was the so-called echo planar imaging and signal targeting by the alternating radiofrequency (EPISTAR) method (58), and shortly thereafter the flow-sensitive alternating inversion recovery (FAIR) technique was introduced (59), which automatically compensates for MT effects (Figure 3). In the slice-selective (ss) experiment, the image is perfusion-weighted and the corresponding magnetisation will be referred to as M^{ss} below, whereas the magnetisation in the non-slice-selective (ns) experiment will be referred to as M^{ns}. FAIR was later combined with 3D-GRASE as a gradient and spin echo readout module that significantly improved the SNR (60). In the studies described in Papers III and IV, the FAIR labelling technique was employed for acquisition of the ASL images, using either 3D-GRASE (Paper III) or echo-planar imaging (EPI) (Paper IV) readout.

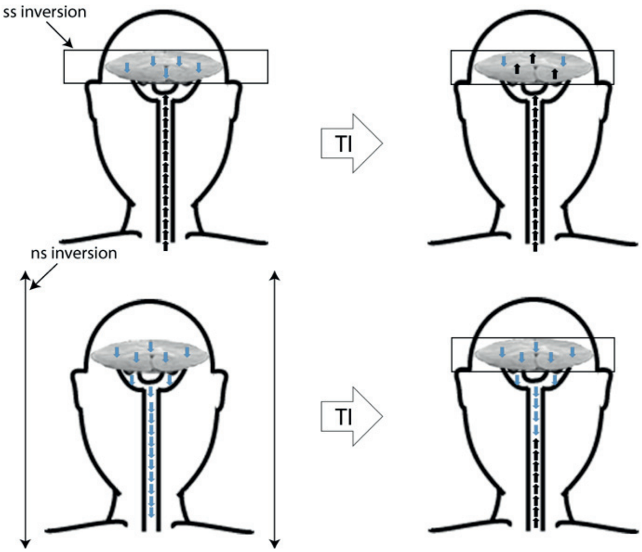

Figure 3:
Labelling scheme in FAIR ASL imaging. The left panel shows the magnetisation immediately after the inversion pulse, whereas the right panel shows the magnetisation immediately before the imaging RF pulse. Blue arrows represent inverted spins and black arrows represent undisturbed spins. In slice-selective (ss) inversion, only spins in the readout slice are inverted, whereas in non-selective (ns) inversion, all spins are inverted.

Recently, pseudo-continuous arterial spin labelling (pCASL) has been used as the technique of choice for perfusion imaging in clinical applications (61). The pCASL is a hybrid of the CASL and PASL techniques. In pCASL, a train of short RF pulses in a narrow labelling plane is used for inverting the arterial spins immediately proximal to the imaging slices, thus minimising signal loss owing to T1 decay of the bolus (62). Comparative studies have demonstrated that pCASL provides quantitative values in accordance with those obtained using the PET technique, which is currently the gold standard (63-65). Another technique that is gaining popularity is velocity-selective ASL (vs-ASL), in which all the upstream blood that is flowing at a velocity above a cut-off value, ideally corresponding to the velocity of the arterioles, is labelled regardless of location (66). In vs-ASL, the sensitivity to transit delay is reduced and CBF quantification is improved (67), but at this point the SNR is a constraining factor, as labelled blood can only be saturated rather than inverted, resulting in a 50% reduction of the ASL signal (68). Qin and van Zijl (69) recently reported the use of a so-called Fourier-transform-based velocity-selective inversion (FT-VSI) pulse train for vs-ASL. It considerably improved the labelling efficiency and resulted in an average SNR value in GM that was 39% higher than in conventional vs-ASL and only 9% lower than in pCASL.

As mentioned above, the difference between the labelled and the control image is directly related to CBF. However, to calculate CBF in absolute terms, a perfusion model describing blood-to-tissue water exchange kinetics and magnetisation characteristics is required. The most widely used kinetic model was presented by Buxton et al. (70). It describes the behaviour of the signal difference in pulsed and continuous/pseudo-continuous ASL experiments.

If the off-resonance and MT effects are the same in both labelled and control images, the signal difference depends only on the difference in tissue longitudinal magnetisation $\Delta M(t)$. This difference is due to (i) arterial inflow of spins in a different magnetisation state from that in static tissue, described by the delivery function $c(t)$, (ii) the venous outflow of labelled spins, described by the impulse residue function $r(t,t')$, i.e. the fraction of labelled spins that arrived at time t' and are still in the voxel at time t, and (iii) the effects of longitudinal relaxation, described by the magnetisation relaxation function $m(t,t')$, i.e. the fraction of the original longitudinal magnetisation carried by arterial water that arrived at time t' and still remains at time t. The magnetisation at time t can then be expressed as a product of the functions above integrated over time until the readout, as follows:

$$\Delta M(t) = 2 \cdot \alpha \cdot M_0^B \cdot CBF \int_0^t c(t')r(t-t')m(t-t')dt' \qquad [13]$$

where α is the labelling efficiency, M_0^B is the MR signal from the fully relaxed arterial blood and the factor 2 corresponds to the use of an inversion RF pulse to label the arterial water.

The Buxton model is based on three assumptions:

1) The labelled arterial water to a particular voxel is assumed to be delivered via uniform plug flow, i.e. no labelled spins arrive before the initial transit delay, the so-called bolus arrival time *BAT*. The arriving bolus is uniformly labelled between $t = BAT$ and $t = BAT + BL$, where BL is the bolus length, and the arriving blood is unlabelled for $t > BAT + BL$; under this assumption, the delivery function *c(t)* can be described by

$$c(t) = \begin{cases} 0 & 0 < t \leq BAT \\ \alpha \cdot e^{-\frac{t}{T_1^a}} \, (PASL) & \\ \alpha \cdot e^{-\frac{BAT}{T_1^a}} \, (CASL/pCASL) & BAT < t \leq BAT + BL \\ 0 & t > BAT + BL \end{cases} \qquad [14]$$

2) The kinetics of water exchange between capillaries and tissue are assumed to be described by a single well-mixed compartment containing both blood and tissue. Hence, $\Delta M^v(t) = \Delta M^t(t)/\lambda$, which implies that the venous concentration of labelled spins $\Delta M^v(t)$ is given by the ratio of the total tissue concentration $\Delta M^t(t)$ to the equilibrium blood-brain partition coefficient λ (defined by Kety (71) as the ratio of the tissue to blood tracer concentrations at equilibrium). Reported values of λ are 0.82 ml/g in white matter and 0.98 ml/g in grey matter (72). With this assumption, the residue function is given by

$$r(t) = e^{-t \cdot \frac{CBF}{\lambda}} \qquad [15]$$

3) After the labelling pulse, the magnetisation relaxes by the relaxation time of blood T_1^a, but as soon as the labelled spins reach the tissue voxel, the magnetisation is assumed to undergo relaxation with the relaxation time of tissue T_1, as the transition of labelled water from the vascular to the tissue space is assumed to occur immediately after the arrival at the tissue voxel. This assumption yields the following relaxation function:

$$m(t) = e^{-\frac{t}{T_1}} \qquad [16]$$

Application of Equations 14, 15 and 16 to the evaluation of the basic model in Equation 13 leads to the following expression for the PASL signal difference:

$$\Delta M(t) = \begin{cases} 0 & 0 < t \leq BAT \\ 2M_0^B \cdot CBF(t - BAT)\alpha \cdot e^{-\frac{t}{T_1^a}} \cdot q_p(t) & BAT < t \leq BAT + BL \\ 2M_0^B \cdot CBF \cdot BL \cdot \alpha \cdot e^{-\frac{t}{T_1^a}} \cdot q_p(t) & t > BAT + BL \end{cases} \qquad [17]$$

where

$$q_p(t) = \frac{e^{kt}(e^{-k \cdot BAT)} - e^{-kt})}{k(t - BAT)} \qquad BAT < t \leq BAT + BL$$
$$q_p(t) = \frac{e^{kt}(e^{-k \cdot BAT} - e^{-k(BL+BAT)})}{k \cdot BAT} \qquad t > BAT + BL \qquad [18]$$

$$k = \frac{1}{T_1^a} - \frac{1}{T_1^{app}} \qquad [19]$$

$$\frac{1}{T_1^{app}} = \frac{1}{T_1} + \frac{CBF}{\lambda} \qquad [20]$$

The model presented by Buxton et al. (70) can describe the behaviour of the signal difference in the ASL experiment but not the separate signal values of the control and label experiments. By using the Bloch equation approach (55), additional information can be extracted from the original ASL data that can be used to stabilise the parameter estimation. The modified Bloch equation, including flow effects, is as follows:

$$\frac{dM^t(t)}{dt} = \frac{M_0^t - M^t(t)}{T_1} + CBF[M^b(t) - M^v(t)] \qquad [21]$$

where M^b, M^v and M^t are the magnetisations of arterial, venous and tissue water per unit volume, respectively. M_0^t is the fully relaxed value of M^t. Moreover, in this case, a well-mixed compartment is assumed, and venous outflow $CBF \cdot M^v$ can be replaced by $\frac{CBF}{\lambda} M^t$. By using the initial condition $M^t=0$ at $t=0$, which is due to proximal saturation, Equation 21 can be solved as follows:

$$M^t(t) = \frac{M_0^t}{1 + CBF \cdot t/\lambda} \left\{ 1 + \frac{CBF \cdot T_1}{\lambda} e^{-\left(t\left(\frac{1}{T_1} + \frac{CBF}{\lambda}\right)\right)} \right\} \qquad [22]$$

As seen in the exponent of Equation 22, the tissue magnetisation relaxes by an apparent time constant $T_1^{app} = 1/\left(\frac{1}{T_1} + \frac{CBF}{\lambda}\right)$, which is equivalent to the relaxation time in Equation [20].

In the slice-selective (ss) experiment, where inflowing blood and tissue in the imaging plane are in different magnetic states, the arterial water magnetisation at equilibrium will be $M^b(t) = \frac{M_0^t}{\lambda}$. Inserting this into Equation 21 yields

$$\frac{dM^{ss}(t)}{dt} = \frac{M_0^t - M^{ss}(t)}{T_1^{app}} \tag{23}$$

Hence, after the slice-selective inversion pulse, the inflowing non-labelled arterial water enters the imaging slice during the time TI and exchanges with tissue spins. This apparently reduces the recovery time of tissue magnetisation and leads to an apparent relaxation time T_1^{app}.

The arterial water magnetisation in the non-slice-selective (ns) experiment will be $M^b(t) = M_0^t/\lambda(1 - 2e^{-t/T_1^b})$, which is inserted into Equation 21 and yields

$$\frac{dM^{ns}(t)}{dt} = \frac{M_0^t - M^{ns}(t)}{T_1^{app}} - \frac{2M_0^t \cdot CBF}{\lambda} e^{-\frac{t}{T_{1a}}} \tag{24}$$

The solutions of the Bloch equations in Equations 23 and 24 provide the magnetisations in the ss and ns experiments, respectively, i.e.

$$M^{ss}(t) = M_0^t - 2\alpha M_0^t e^{-\frac{t}{T_1^{app}}}$$
$$M^{ns}(t) = M_0^t - 2\alpha M_0^t e^{-\frac{t}{T_1}}$$

The magnetisation difference $\Delta M(t) = M^{ss}(t) - M^{ns}(t)$ thus corresponds to the Buxton approach in Equation 17, which was used to calculate CBF values in Paper IV.

Chapter 4

Noise characteristics

4.1 Signal and noise in MRI

Low SNR is a well-known issue in MRI, and noise can be a major disadvantage, particularly in applications based on signal reduction, such as DWI and DSC-MRI (i.e. bolus-tracking T_2* and T_2-weighted perfusion MRI). Furthermore, ASL techniques suffer from inherently low SNR owing to the small amount of labelled blood in the voxel, which determines the signal difference, and to the rapid T_1 relaxation of the endogenous tracer. Noise is problematic in other applications as well, where averaging is prohibited by temporal-resolution requirements, for example, in dynamic time-series used for functional MRI (fMRI). The issue of noise in MRI data was discussed already in the early days of MRI (73), and a quantitative description of the noise distribution was presented.

MR images are reconstructed from signal data measured by a receiver coil detector system and sampled in the spatial-frequency or k-space domain. When quadrature detection is employed, the acquired k-space data (sometimes referred to as raw data) are collected in two channels (often referred to as the real and the imaginary signal components), and both these data components are considered to be affected by additive Gaussian noise (73,74). The major source of this noise is random thermal noise from the patient, whereas additional noise arises from the acquisition hardware.

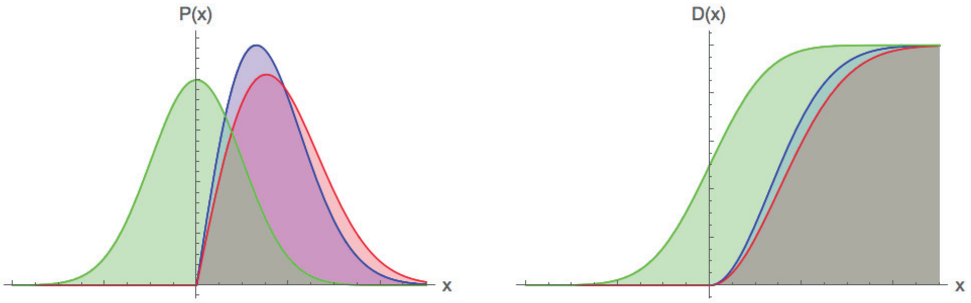

Figure 4:
Probability functions P(x) of Gaussian of mean 0 and SD = 1 (green), Rayleigh of SD = 1 (blue) and Rice distribution of mean 1 and SD = 1 (blue), and their corresponding cumulative functions D(x).

A Gaussian distribution (Figure 4:) of a random variable x with mean ⍰ and variance σ^2 is given by the following equation:

$$P(x) = \frac{1}{\sigma\sqrt{2\pi}} e^{-(x-\mu)^2/(2\sigma^2)} \text{ on } x \in (-\infty, \infty) \qquad [25]$$

The reconstruction of MR images is normally accomplished using a two-dimensional (2D) Fourier transformation of the k-space data. The Fourier transform preserves the shape of the noise distribution, which remains Gaussian. The MR images are normally converted to magnitude images (M) by calculating the absolute value pixel by pixel from the real and the imaginary images, namely,

$$|m(i,j)| = [(s(i,j)\cos(\varphi) + n_{Re}(i,j))^2 + (s(i,j)\sin(\varphi) + n_{Im}(i,j))^2]^{\frac{1}{2}} \qquad [26]$$

where $|m(i,j)|$ is the signal magnitude in pixel (i,j), $s(i,j)$ is the true signal, φ is the phase angle, and n_{Re} and n_{Im} are the noise contributions to the real (Re) and imaginary (Im) parts of the given pixel (i,j), respectively.

From Equation 26, it is seen that the construction of M involves both the true signal and the noise, leading to a modified noise distribution and, of course, loss of all information about the phase angle φ.

The noise in M is signal dependent and follows a Rician distribution (73-76) (Figure 4) whose probability function is given by

$$P(m) = \frac{m}{\sigma^2} e^{-(m^2+s^2)/2\sigma^2} \hat{I}_0\left(\frac{s \cdot m}{\sigma^2}\right) \text{on } m = [0, \infty) \qquad [27]$$

where $\hat{I}_0$ is the modified zeroth-order Bessel function of the first kind (77). If the true signal $|s| = 0$, Equation 27 reduces to a Rayleigh distribution (Figure 4) given by

$$P(m) = \frac{m}{\sigma^2} e^{-m^2/2\sigma^2} \text{on } m = [0, \infty) \qquad [28]$$

The probability and cumulative functions of the Rician distribution are intermediate between the Rayleigh distribution and the Gaussian distribution. If the true signal $s \to 0$, then (Rician distribution)→(Rayleigh distribution), whereas if $s \to \infty$, then (Rician distribution)→(Gaussian distribution). If SNR is below approximately 2, the noise distribution cannot be accurately approximated by a Gaussian function (74).

In the absence of any true signal, the mean (η) and standard deviation (σ_η) of the signal magnitude are given by

$$\eta = \sigma\sqrt{\frac{\pi}{2}} \text{ and } \sigma_\eta = \sigma\sqrt{2 - \frac{\pi}{2}} \qquad [29]$$

where σ is the standard deviation of the MR signal in the real and imaginary channels (assumed to be equal in both channels) (15). This results in a non-zero minimum mean signal in the magnitude image, sometimes referred to as the rectified noise floor (15).

For multichannel coil systems, the noise distribution in reconstructed images becomes more complex and can be described by a non-central Chi distribution (78). Moreover, when parallel imaging techniques are employed, the noise amplitude varies spatially across the image. Such spatial noise variations are particularly pronounced in the sensitivity encoding (SENSE) technique (79), whereas the generalised autocalibrating partially parallel acquisitions (GRAPPA) approach (80) exhibits a more uniform spatial distribution (81). The SNR observed for each coil element in SENSE (denoted by SNR_{SENSE} below) is decreased compared with the SNR of a fully sampled k-space, SNR_{conv}. That is,

$$SNR_{SENSE} = \frac{SNR_{conv}}{g\sqrt{R}}, g \geq 1 \qquad [30]$$

where *g* is the geometry factor, which reflects the suitability of the employed coil array for distinguishing signal contributions from the originally aliased location, and depends on the shape, size and placement of the coil elements. *R* is the reduction factor, describing the reduction in the number of Fourier encoding steps. Theoretically, the reconstruction would be performed by using *R* values up to the number of coils, but in practice *R*, is limited by *g*, which increases with *R* (79).

Physiological noise

At higher field strengths, image quality is further degraded by non-white physiological noise, which arises from fluctuations in metabolic-linked physiological processes and from brain and CSF pulsations. The physiological noise is signal dependent and increases at the same rate as the signal. At some point, the achievable SNR reaches an asymptotic limit, owing to the physiological noise contribution (82).

4.2 Noise in diffusion MRI

As mentioned earlier, noise has a negative impact on DWI and DTI, and low SNR makes various types of quantitative analyses more problematic. A major issue is the systematic increase in mean signal intensity caused by the rectified noise floor at high b-values, leading to overestimation of the DW signal amplitude. In DTI, the diffusion displacement distribution is usually described by a Gaussian function (83). If DW images are acquired at moderate spatial resolution (e.g. a voxel size of 2.5 mm^3) and moderate diffusion weighting ($b < 1000$ s mm^{-2}), a voxel containing multiple fibre populations (e.g. so-called kissing or crossing fibres) is characterised by a tensor whose associated ellipsoid is not prolate and may become spherical or even oblate. In such cases, the Gaussian tensor model fails to adequately describe the underlying tissue microstructure, and this can be problematic for applications such as fibre tracking (15). To describe such complex tissue structures, advanced DWI methods are required, for example, q-space imaging (84), high-angular resolution methods (85), diffusion kurtosis imaging (DKI) (50,51), mean apparent propagator MRI (MAP-MRI) (86) and, more recently, neurite orientation dispersion and density imaging (NODDI) (87). Such techniques are often based on the application of high gradient amplitude and/or long diffusion time, i.e. high b-values, which leads to substantial attenuation of the measured MR signal. Several clinical MRI systems have insufficient gradient strength, and this is sometimes compensated for by the use of longer gradient pulse widths (88), which, however, prolongs the echo time and causes additional signal decrease owing to T_2 relaxation. Furthermore, the choice of pulse-sequence type is also relevant for the resulting SNR. Gradient-echo (GRE) (although rarely used in DWI) and stimulated-echo (STEAM) pulse sequences, for example, tend to produce images with lower SNR than spin-echo pulse sequences.

The demand for higher SNR has been highlighted in several studies. Clark & Le Bihan (89) argued that higher SNR was required for reliable biexponential fitting of data on a pixel-by-pixel basis to separate the slow and fast diffusion components, and Anderson noted that noise has a substantial impact on MR fibre tracking results (90). When higher spatial resolution is required to resolve fine anatomic structures, noise also becomes a limitation (15). In Paper I, a wavelet denoising algorithm was proposed that can potentially alleviate these issues.

4.3 Noise in ASL

As previously mentioned, ASL measurements generally suffer from low SNR, owing to the small amount of labelled spins affecting the tissue signal in the labelling experiment, as well as to the comparatively short relaxation time of the arterial water magnetisation. Under ideal circumstances, CASL techniques provide higher SNR than PASL; however, despite the higher measured signal in CASL experiments, the SNR per unit time, which is a more relevant quantity than absolute SNR, is practically identical for both techniques (91). SNR is typically further decreased in techniques aimed at absolute CBF quantification, such as QUIPSS (92) and Q2TIPS (93), owing to the saturation of a certain fraction of the labelled water, which is performed to control the width of the labelled bolus. The SNR of data acquired in pCASL is usually higher than in PASL, but the inversion efficiency may be affected by off-resonance spins, and the technique is susceptible to B_0 inhomogeneity and eddy currents (67). As shown in Figure 5, the noise distribution resulting from subtracting two noisy images, label (*L*) and control (*C*) (both exhibiting Rician noise distributions), is symmetric and can be well approximated by a Gaussian distribution for all SNR levels (94).

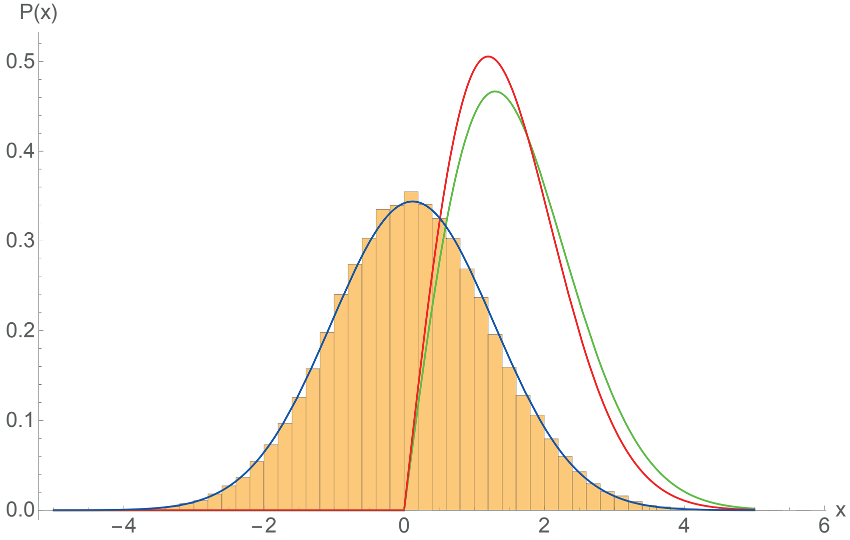

Figure 5:
Probability density functions for a variate x of two Rician distributions with SNR = 1.3 (green) and 1.2 (red), and the corresponding histogram of the difference between them (yellow). The distribution of the difference is compared with the fitted probability density function of a Gaussian distribution (blue).

To improve SNR in ASL, multiple averaging is usually performed, corresponding to a series of temporally interleaved L and C images. To extract the averaged difference signal $\langle \Delta M \rangle$, the C and L images are usually subtracted according to the following equation, which is the standard method for creating difference maps:

$$\langle \Delta M \rangle = \frac{[(C_1 - L_1) + (C_2 - L_2), \ldots, (C_N - L_N)]}{N} \qquad [31]$$

where N is the number of averages. The so-called 'surround subtraction' is sometimes used, where the difference between each image and the average of its two closest neighbours is calculated (95) as follows:

$$\langle \Delta M \rangle = \frac{[(C_1 - L_1) + (C_2 - \frac{L_1 + L_2}{2}), \ldots, (C_N - \frac{L_{N-1} + L_N}{2})]}{N} \qquad [32]$$

Another approach is sinc-interpolated control and label images (96) (Equation 33), accomplished by doubling the temporal resolution of the label images using sinc interpolation (where every new label image at the intermediate point is created by averaging the two closest label images) and, finally, resampling at the intermediate points in time. This can be a better option if ASL is used in, for example, perfusion fMRI studies to minimise BOLD contamination effects.

$$\langle \Delta M \rangle = \frac{[(C_1 - L_{1/2}) + (C_2 - L_{3/2}), \ldots, (C_N - L_{N-1/2})]}{N} \qquad [33]$$

The standard deviation $\sigma_{\Delta M}$ in $\langle \Delta M \rangle$, calculated by the standard method in Equation 31, is given by

$$\sigma_{\Delta M} = \frac{\sqrt{\sigma_{C_1}^2 + \sigma_{L_1}^2 + \sigma_{C_2}^2 + \sigma_{L_2}^2 + \cdots + \sigma_{C_N}^2 + \sigma_{L_N}^2}}{N} = \frac{\sqrt{N \cdot \sigma^2}}{N} = \sqrt{\frac{2}{N}} \cdot \sigma \qquad [34]$$

where σ is the standard deviation of the Rician distribution, assumed to be equal in all L and C images. The SD in the difference maps acquired according to Equation 32 is given by

$$\sigma_{\Delta M} = \frac{\sqrt{\left(\sigma_{C_1}^2+\sigma_{L_1}^2\right)^2+\left(\sqrt{\sigma_{C_2}^2+\left(\frac{\sqrt{\sigma_{L_1}^2+\sigma_{L_2}^2}}{2}\right)^2}\right)^2+\left(\sqrt{\sigma_{C_N}^2+\left(\frac{\sqrt{\sigma_{L_{N-1}}^2+\sigma_{L_N}^2}}{2}\right)^2}\right)^2}}{N} = \frac{\sqrt{(1+3N)}}{\sqrt{2}N}\cdot\sigma \qquad [35]$$

The noise distribution in the averaged difference image ΔM is still symmetric and can, as stated above, be approximated by a Gaussian distribution.

Although ASL data suffer from intrinsically low SNR, denoising algorithms have not been frequently applied. However, in Paper I, a denoising filtering method was proposed, which was subsequently applied to ASL data, as reported in Paper II, where an investigation of the performance of the denoising algorithm and a comparison with Gaussian smoothing were performed.

Chapter 5

Denoising methods

5.1 Filtering methodologies

In all denoising methods, the aim is to decrease the noise contributions to the measured signal without compromising important the 'true' signal. Gaussian filtering is a commonly used filtering method that effectively reduces noise but also tends to spatially blur the image data. Another spatial filter is the Wiener filter, which introduces adaptive signal smoothing, depending on the local distribution of pixel values within each kernel. To minimise blurring and to preserve image contrast, several different approaches have been presented. For example, the anisotropic diffusion (AD) filter has been shown to improve the reliability of CBF measurements using DSC-MRI (97). Furthermore, a variety of edge-preserving, wavelet-based denoising methods have been proposed following the very first applications of wavelet-based filtering methods to MR images (98,99). Assuming a Gaussian noise distribution in the spatial domain, Donoho et al. (100) suggested a soft-threshold filter and Chipman et al. (101) proposed a Bayesian approach to shrinkage of the wavelet coefficients. Nowak et al. (102) presented a wavelet-domain filtering algorithm that provided effective removal of Rician noise at low SNR from squared magnitude images. Wavelet-domain filtering has also been used to improve fMRI analysis (103) and DSC-MRI data (104).

5.1.1 Gaussian smoothing

Gaussian smoothing is a spatial filter that blurs the pixel values under a filter mask consisting of a Gaussian function. Mathematically, this operation constitutes a convolution of the image with the Gaussian function.

5.1.2 Independent component analysis

Independent component analysis (ICA) is an unmixing technique designed to extract the separate signal components from measurements consisting of a mixture of statistically independent observations (105). Filtering by ICA can be carried out by distinguishing the random noise component and extracting it from the total signal.

5.1.3 Wavelet-domain filtering

The description below is an overview of the wavelet-domain filtering procedures introduced in Papers I and II. In general terms, the image signal is given by

$$x = s + n \tag{36}$$

where s is the noise-free signal and n is Gaussian noise of variance σ^2. After the discrete wavelet transform of noisy data, the corresponding wavelet coefficients can be obtained as follows:

$$y = \theta + z \tag{37}$$

where $y = W_n x$, $\theta = W_n s$ and $z = W_n n$, and W_n denotes a wavelet transform.

The noise distribution in wavelet space remains unchanged because an orthogonal wavelet will transform white noise into white noise, and the noise is uniformly spread over all wavelet coefficients.

To obtain $\hat{\theta}$ of the (i, j)-pixel (i.e., the filtered signal in the wavelet space), each noisy wavelet coefficient is thresholded by multiplication of the wavelet coefficients $y(i,j)$ by the hard-threshold filter $h_h(i,j)$, that is,

$$\hat{\theta}(i,j) = y(i,j) \cdot h_h(i,j) \tag{38}$$

The hard threshold filter H_h sets any $|y(i,j)|$ below $\rho\sigma$ to zero and keeps the remaining data unchanged, i.e. the filter is given by the following expression:

$$h_h(i,j) = \begin{cases} 1, & \text{if } |y(i,j)| > \rho\sigma \\ 0, & \text{otherwise} \end{cases} \tag{39}$$

where ρ is a user-defined empiric threshold factor and σ is the standard deviation of the noise.

Larger values of ρ typically result in greater noise reduction; however, they lead to image smoothing and artefacts. Hence, optimisation of this threshold factor is required. The standard deviation σ can be obtained from the finest-scale wavelet coefficients. Filtered signals can then be obtained as follows:

$$\hat{s} = W_1^{-1} H_h W_1 x \qquad [40]$$

An overview of this part of the filtering procedure is given by the block diagram in Figure 6.

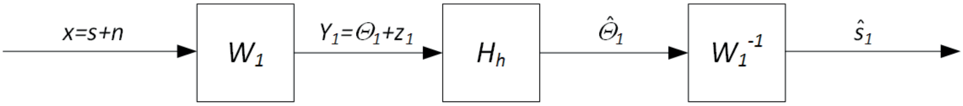

Figure 6:
Block diagram of the initial wavelet-domain filtering. The wavelet transform W_1 was used to transform a signal into the wavelet space, and the hard-threshold filter H_h was applied to signal y_1. The inverse wavelet transform W_1^{-1} was used to reconstruct the filtered signal $\hat{\theta}_1$ to the signal $\hat{s}_1$ in the complex image space.

To further improve the estimated data $\hat{s}_1$, a Wiener-like filter H_W can be employed to shrink each wavelet coefficient $\hat{\theta}(i,j)$ by a factor $h_w(i,j)$ given by

$$h_w(i,j) = \frac{|\theta(i,j)|^2}{|\theta(i,j)|^2 + \sigma^2} \qquad [41]$$

The Wiener-like filter requires knowledge of the signal and its noise properties. The variance σ^2 can be estimated from the finest-scale wavelet coefficients according to the description above. However, $\theta(i,j)$ is the noise-free signal in the pixel (*i,j*), i.e. the unknown signal to be retrieved. At this point, the closest approximation is to use the hard-threshold filtered data. Equation 41 is then modified as follows:

$$h_w(i,j) = \frac{\left|\hat{\theta}(i,j)\right|^2}{\left|\hat{\theta}(i,j)\right|^2 + \sigma^2} \qquad [42]$$

From this equation, it is seen that the filter has the highest effect at small $\theta^2(i,j)$ compared with σ^2, and its effect decreases monotonically when $\theta^2(i,j) \to \infty$ and

$h_w(i,j) \rightarrow 1$. Consequently, the Wiener-like filter does not primarily affect the large scaling or wavelet coefficients, but it does influence the small ones.

Furthermore, the hard-threshold filtered data should be transformed from the image space to the wavelet space with a different wavelet family before the second filtering because different wavelet transforms decompose the noise from the signal differently.

$$\hat{\theta}_{21} = W_2 \hat{s}_1 \qquad [43]$$

With the estimated data $\hat{\Theta}_{21}$, the Wiener-like filter can be constructed and applied to the hard-threshold filtered data (see the block diagram in Figure 7).

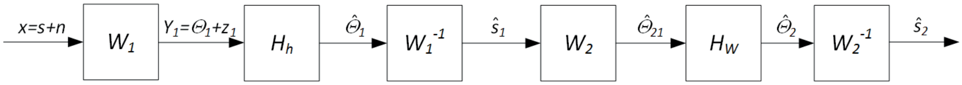

Figure 7:
Block diagram of wavelet-domain filtering. The wavelet transform W_1 was used to transform the signal x into the wavelet space, and the hard-threshold filter H_h is applied to signal y_1 to produce the pilot signal $\hat{s}_1$. This estimate can then be used to construct the Wiener-like filter H_w in the W_2 domain, which is applied to the pilot signal $\hat{s}_1$.

To achieve additional reduction of the standard deviation and the mean signal of the background, the estimated value $\hat{s}_2$ is used to construct a new Wiener-like filter that is applied to the original noisy signal x according to Figure 8. This approach is an extension of the so-called WienerChop technique (106).

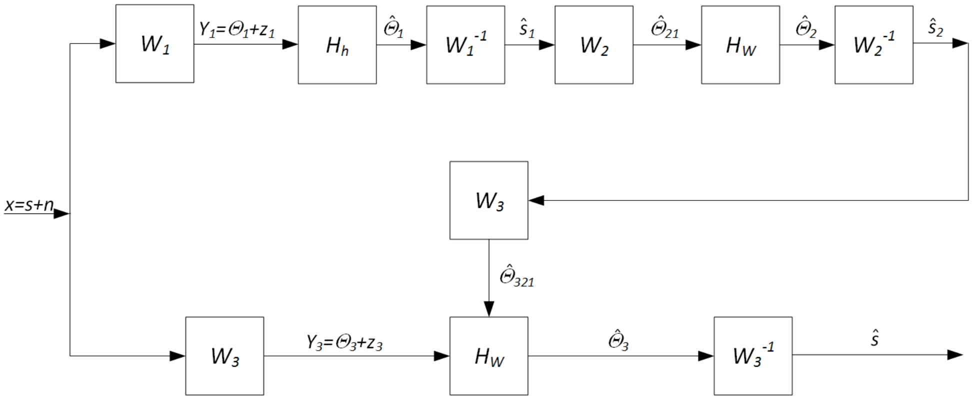

Figure 8:
Block diagram of the complete wavelet-domain filtering procedure. The top row is the same as in Figure 7. The addition here is that the estimated signal is used to construct another Wiener-like filter applied to the original noisy signal x in the W_3 domain.

5.1.4 Extensions of the wavelet denoising concept

Various other wavelet-like transforms have been proposed for denoising. One example is the curvelete transform (107), which is associated with a transform that tends to decompose the edges in the signal considerably more efficiently than wavelets, and thereby it better retains edge information after filtering. Another example is the contourlet transform (108), which provides not only multi-resolution expansion of images but also directional, which would be useful for denoising of multi-dimensional data. A more detailed analysis of these transforms is, however, beyond the scope of this thesis.

5.2 Filtering for noise reduction in diffusion MRI

In several cases, the best approach to improve SNR in MRI is to acquire multiple datasets and apply averaging. In DWI, signal averaging is not always practical owing to time constraints, and it is important to notice that averaging in the image domain does not solve the problem of rectified noise floor because signal intensities are always biased for SNRs lower than approximately 2 (74). To minimise the effects caused by the noise floor, relatively large voxel sizes have been used in various in vivo studies, impairing the image spatial resolution. In other cases, high b-values have been omitted to ensure that noise-floor-related artefacts are not manifested, but this may result in loss of important diffusion information.

Other methods for increasing SNR include using surface coils (to get closer to the object) and stronger diffusion gradients (enabling shorter TE and correspondingly increased SNR) (15). In addition, the noise and the noise floor can be further reduced by post-processing, without improved hardware or prolongation of the scan time.

To minimise blurring and to preserve image contrast in DWI images, several different approaches have been presented, for example, filtering applied to diffusion tensor MRI by using anisotropic smoothing along structure boundaries (109), separating and removing the noise by ICA (110), or using nonlinear smoothing techniques for reducing both random and systematic errors (111).

Wavelet filtering after 2D Fourier transform of k-space data and before construction of the magnitude images has previously been presented (112), and in the study reported in Paper I, an improved wavelet-domain Wiener-like filter (106) was applied to data in the complex image domain.

The output from wavelet-domain filtering of a simulated signal, degraded by Rician noise, is shown in Figure 9, where the mean signal as a function of b-values in a high diffusivity ($ADC_2 = 1.0 \cdot 10^{-3}\ mm^2 s^{-1}$) area as well as in the background are depicted. The noise floor (represented by the signal in the background) was reduced by a factor 6–7, and the useful number of b-values was at least doubled in this particular case.

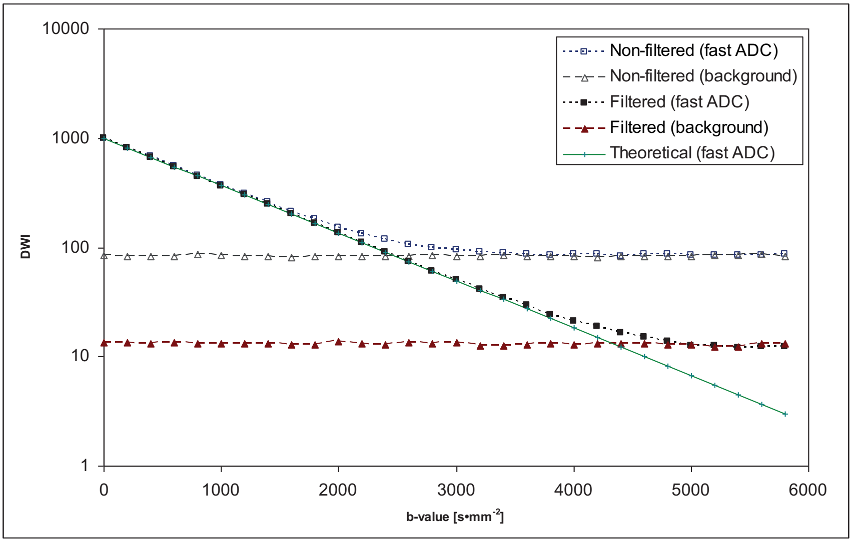

Figure 9:
Mean values of simulated diffusion-weighted signal intensities in a fast ADC region ($ADC_2 = 1.0 \times 10^{-3}\ mm^2 s^{-1}$) as well as the mean signal in the background as a function of b-value.

The estimation of simulated bi-exponential signal decay (Equation 44) was significantly improved after filtering, in line with the requirements stated by Clark & Le Bihan (89).

$$DWI(b) = Ae^{-bADC_A} + Be^{-bADC_B} \quad [44]$$

The parameters in the simulated bi-exponential data were A = 680, B = 1000 − A = 320, $ADC_A = 1.25 \cdot 10^{-9}$ m^2/s, $ADC_B = 0.18 \cdot 10^{-9}$ m^2/s, and the SNR at b = 0 was 15 (113). Recently, the kurtosis model (50,51) and other approaches related to non-Gaussian diffusion have been increasingly used to account for the deviation from a mono-exponential signal decay at high b-values, and these models have also been shown to be sensitive to noise, particularly the kurtosis fractional anisotropy parameter (K_{FA}) (114). However, noise floor effects are not evident for parameters associated with the NODDI model, possibly because noise effects are accounted for as a part of the implementation of the NODDI model (115).

For experimental data, the DW signal quality in images of a homogeneous phantom was markedly improved after filtering, as seen in Figure 10.

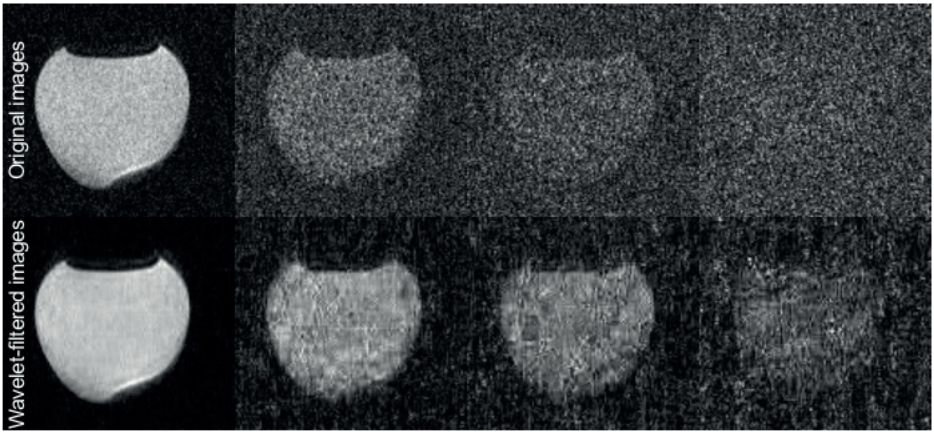

Figure 10:
Original and wavelet-filtered images of a n-decane phantom (diffusion coefficient approximately $1.3 \cdot 10^{-3}$ mm^{2}s^{-1} at 20°C) at different SNR levels (b-values, from left to right ranging from 0 to 1617 s/mm^2). For each image pair, the original image is in the top row and the corresponding denoised image is in the bottom row.

Furthermore, filtering also resulted in improved in vivo FA data. FA based on b-values in the range from 0 to 930 s/mm^2 decreased, primarily in low-anisotropy regions, when denoising was applied: FA recorded from regions of interest (ROIs) in low-anisotropy regions (peripheral grey matter/cerebrospinal fluid) was reduced from 0.27 to 0.18, whereas white-matter FA values were reduced only from 0.75 to 0.71, i.e. approximately 31% and 6%, respectively (Figure 11).

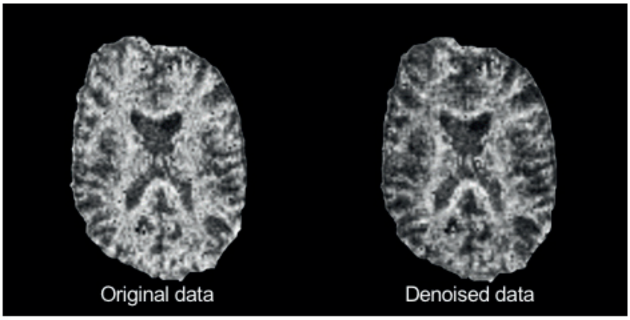

Figure 11:
FA maps from a healthy volunteer, calculated using b-values in the range 0-930 s/mm^2. Left: Original data. Right: Denoised data. Background noise was removed by masking.

As noted above, the noise in k-space data and in the corresponding complex image domain is assumed to follow a zero-mean Gaussian distribution with equal variances in the real and imaginary parts. This is a prerequisite for the proposed filtering method (reported in Papers I and II).

Hence, the proposed filter should also be applicable to coil systems with multiple channels, but only if data from each coil are handled separately. The filtering method was not evaluated for data acquired by parallel imaging techniques (e.g. SENSE (79) or GRAPPA (80)) that were shown to exhibit more complicated noise distributions. The subsampling of k-space data in parallel imaging affects the distribution of the noise in reconstructed data (116), but for each coil element, the noise distribution should still be zero-mean in k-space and in the corresponding complex image domain. Hence, the filtering method should still be applicable to data taken from a separate coil.

5.3 Filtering for noise reduction in ASL

Achieving an adequate SNR level in ASL at a suitable spatial resolution normally requires averaging of a large number of ASL images (typically of the order of 40−100 images) (93,117-119). However, this can be problematic in clinical MRI owing to the long acquisition time and increasing sensitivity to motion artefacts (120). Lower noise or increased SNR would obviously reduce the required number of averages, and several approaches have been proposed to achieve this, mainly to increase the intrinsic signal: (i) Higher magnetic field strength increases the SNR and prolongs the T_1 relaxation time, which may directly improve ASL quality owing to the slower decay of the labelled arterial blood water (121). (ii) Increasing the receiver coil efficiency can boost the SNR in ASL. (iii) Ferré et al. reported that a 32-channel array head coil performs considerably better in terms of SNR than a 12-channel coil (122). (iv) Improved SNR can be achieved by exploring alternative ASL techniques: For example, Ye et al. (123) and Günther et al. (60) suggested 3D sequences for data acquisition (employed in the study described in Paper III), Wong et al. used a so-called Turbo ASL sequence to obtain higher temporal resolution and higher SNR per unit time (124), and Jahanian et al. proposed a method utilising B_0 field map information to compensate for the loss in tagging efficiency in pseudo-continuous ASL, thus effectively recovering SNR (125).

However, the use of noise-reduction algorithms in ASL has been sparse, and such techniques have mainly been restricted to the minimisation of fluctuations in signal intensity due to physiological noise and have been mostly applied to ASL-fMRI studies (126-129). In Paper II, an implementation of two denoising techniques was reported, evaluated using simulations and applied to human ASL data acquired by a clinical MR scanner. Conventional Gaussian smoothing was compared with a wavelet-domain filtering method, focusing on the effects of denoising on accuracy, precision and structural degradation at different noise levels ($4 \leq \text{SNR} \leq 12$). It was shown that wavelet-domain filtering was superior to Gaussian smoothing in the vicinity of borders between grey and white matter and close to edges of the object, particularly at moderate to high SNRs. Gaussian smoothing causes a well-known loss of object detail, which is a considerable disadvantage in ASL applications owing to the relatively low resolution, being of the same order of magnitude as the size of the human sulcus. In this context, it is important to point out that both denoising techniques introduced a bias in areas close to the edges and borders, but the bias introduced by wavelet-domain filtering remained within the standard deviation of the non-filtered signal.

Figure 12 shows the ASL-weighted signal maps before (non-filtered) and after (Wavelet-filtered) image denoising by wavelet-domain filtering and after Gaussian smoothing. It can be observed that Gaussian smoothing, unlike wavelet-domain filtering, introduced a high degree of spatial smoothing, where some details completely disappeared.

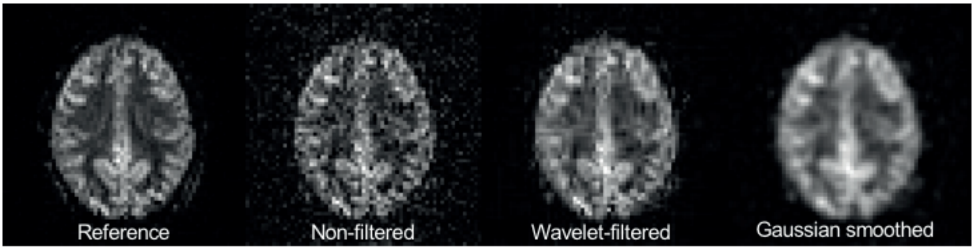

Figure 12:
From left to right: Reference image computed from 300 difference images, non-filtered image computed from five experimental difference images (SNR = 4), wavelet-domain filtered image and Gaussian smoothed image (FWHM = 5.6 mm).

In 2010, Wells et al. (130) performed a similar investigation, including additional spatial denoising techniques, such as Wiener filtering applied in the spatial domain instead of the wavelet domain, a so-called AD filter (131), a Gaussian smoothing filter, simpler wavelet filters including soft and hard thresholding schemes (100), as well as ICA (105). The influence of denoising techniques on both random and systematic errors was investigated with regard to CBF and arterial transit time estimates. In agreement with the findings of the study reported in Paper II, they concluded that different denoising techniques introduce different degrees of spatial smoothing, and that the optimal filter is highly dependent on the SNR and the contrast of the images. However, this research group also found that the ICA method reduced random noise with minimal structural degradation and was superior to wavelet-domain filtering; however, it should be noted that they used a simpler wavelet approach than that used in Paper II.

In summary, image denoising improves the accuracy of ASL estimates, with some decrease in precision in areas close to borders and edges; however, the use of edge-preserving filtering techniques, such as wavelet-domain or ICA, can improve accuracy in these areas. If the wavelet-domain filter is overly aggressively thresholded, some structural degradation in the images may appear. It should also be noted that the method reported in Paper II was used to improve SNR in the studies described in Papers III and IV and should also be directly applicable to other ASL applications, such as model-free ASL using QUASAR (132) or two-compartment models (133), which are normally of limited use owing to their noise sensitivity.

5.4 Possible limitations and sources of error

The major drawback of the proposed approach in the denoising of diffusion images is that it requires the raw image data (k-space data) as well as knowledge of the reconstruction algorithm used to generate the images, i.e. the transform from k-space to the image domain. Furthermore, the proposed filtering method reduces only the contributions of random noise. The physiological noise issue, which is, in practice, always present in MR images, will usually not be rectified by filtering.

Chapter 6

Non-compartment ASL Data modelling

6.1 Background

In Section 3.2, a simple single-compartment model was described (70), enabling absolute quantification of CBF, an important indicator of tissue viability and function, and also returning the arterial transit time (ATT), which may be an additional important parameter, potentially reflecting hemodynamic impairment in cerebrovascular disease (134). However, the labelled arterial blood water distributes over several different compartments before image acquisition, and the estimation of parameters describing the delivery to different compartments may lead to better characterisation of neurological and neurovascular diseases.

The single-compartment model assumes that labelled water exchanges instantaneously across the blood-brain-barrier. However, by a variety of techniques, it has been shown that water is not a freely diffusible tracer in the brain (41,52-54). To incorporate this condition into the quantification, a multi-compartment analysis is usually required. The brain tissue can be separated into two main compartments: (a) the intravascular compartment (IC), which is subdivided into arterioles, capillaries and venules, and (b) the extravascular compartment (EC), which is subdivided into the intracellular and extracellular tissue spaces (Figure 13) (135,136).

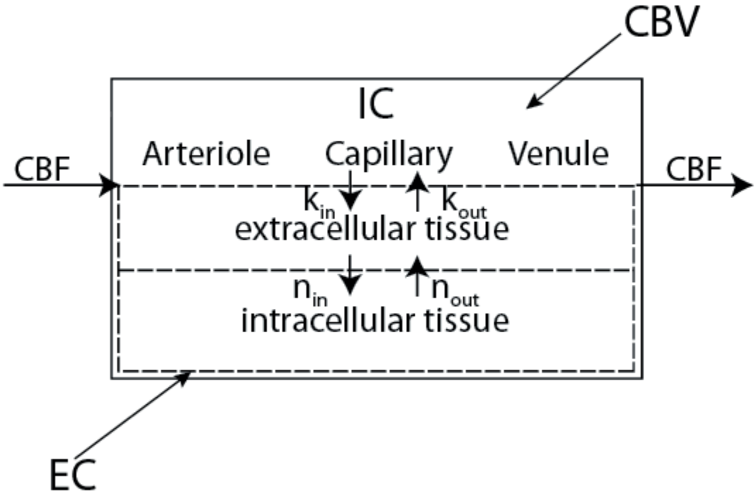

Figure 13:
Schematic three-compartment perfusion model for brain tissue. IC is the intravascular compartment with arterioles, capillaries and venules as sub-compartments, making up the total CBV. EC is the extravascular compartment with the extracellular and intracellular spaces as sub-compartments. The exchange rates between IC and EC are denoted by k, and the exchange rates between the sub-compartments within the EC are denoted by n.

To distinguish water residing in different compartments, several approaches have been presented. For example, Silva et al. (53) combined ASL with intravoxel incoherent motion (IVIM) measurements to obtain the exchange of labelled blood water with tissue water. It was assumed that labelled water resides either in the EC (where it moves by an ordinary diffusion process, characterised by the diffusion coefficient D) or in the IC (where motion is characterised by a pseudo-diffusion coefficient D* related to the sum of the diffusion and the flow of blood in a randomly oriented microvasculature). The blood flow in the IC leads to D* becoming significantly larger than D in the EC, and the DW signal is thus attenuated significantly faster in the IC than in the EC. ASL images were acquired at different b-values and, according to the IVIM model, it was possible to separate the fraction of labelled water that remained in the IC from the fraction that exchanged with the EC by fitting ASL data to the bi-exponential expression as follows:

$$\frac{\Delta S(b)}{\Delta S(0)} = (1-A)e^{-bD^*} + Ae^{-bD} \qquad [45]$$

where A is the fraction of the slow component, which would be equal to the extraction fraction of water if the ASL signal contribution of the slow component were to be composed of extravascular spins only.

Further studies have shown that the transverse relaxation time T_2 differs among different compartments, with T_2 in the IC being shorter than in the EC (137-139). This allowed the estimation of the ASL signal distribution between the two compartments IC and EC, but also in the two sub-compartments within the EC by estimating the T_2 values of the intra- and extracellular tissues from the control images by applying vascular crusher gradients and fitting to a biexponential model using different tagging pulse durations (140). This approach was later extended to include the transfer time $T_{IC \to EC}$ of labelled water across vascular walls or the BBB by using multi-TE and multi-TI ASL measurements (141). The 2D model was then fitted to the measured ASL signal by using five degrees of freedom in the fitting algorithm, i.e. CBF, BAT, $T_{IC \to EC}$, T_2^{EC} and T_1^{EC}, whereas BL, T_2^b, T_1^b and αM_0^b were kept fixed. This is obviously a highly complex model with few assumptions, and it is highly unstable owing to the complexity and the uncertainty associated with multiparameter fitting, despite the use of least-squares optimisation routines from MINUIT (142), which is considered to be robust.

Over the years, several different approaches have been proposed for the differentiation of the ASL signal components from different compartments, for example, tracer-kinetic two-compartment exchange models (133,136), diffusion-weighted ASL measurements (134,143,144), and the use of MT effects to shorten the effective T_1 of the EC and make it more distinct from the T_1 in the IC (145).

6.2 Modelling for retrieval of additional hemodynamic parameters

As pointed out in Section 6.1, the idea to measure additional hemodynamic or microcirculatory parameters with ASL is not new. However, several previous reports have stated that the implementation of the models was limited by low SNR, long acquisition time (owing to additional data collection), and/or uncertainties caused by the fitting procedure. A model with short acquisition time, allowing the extraction of additional physiological parameters using data from an ordinary time-resolved ASL experiment, would obviously be more appropriate for clinical applications. Furthermore, stable estimates are desirable, potentially achieved by using simpler modelling assumptions, robust fitting algorithms and increased SNR. In the study reported in Paper III, the non-compartment model and animal ASL methodology by Kelly et al. (146) was modified and adapted to human volunteers in a clinical MRI environment. Additionally, SNR was improved by the wavelet-domain filtering approach presented in Papers I and II. As further detailed below, hemodynamic parameters, i.e. the ATT and the capillary transfer time (CTT), were measured in two ROIs, namely, the occipital lobe (OC) and the insular cortex (ICx), and were compared with literature values of the corresponding parameters measured by other techniques. The impact of the stochastic thermal noise on the model estimates was also investigated, and an appropriate SNR level was established. In Paper IV, the use of a measured AIF, i.e. an AIF of arbitrary shape, was introduced as a further development of the non-compartment model, and this was hypothesised to improve the definition of the labelled bolus and thus the accuracy of the CTT and ATT estimates.

The basic assumption of the non-compartment model (146) is that labelled water is driven by a potential difference in large vessels, which causes the bulk flow, and when arriving at the microvascular space it distributes owing to the random nature of pseudo-diffusion in capillaries, and finally, it exchanges between the capillary bed and the extravascular water through the BBB. Hence, the transport mechanism of labelled spins from the labelling point to the imaging plane can be described by the general Langevin equation as follows:

$$\frac{dV}{dt} = F(V) + \Gamma(t) \tag{46}$$

where V is any volume into which labelled spins can flow, F is the bulk flow rate in the volume V describing an advective transport of a substance not including diffusion of labelled spins, and Γ is the term describing the diffusion transport of labelled spins by a simple Gaussian distribution with zero mean. The first term F on the right-hand side describes the transport in large vessels, and the second term Γ describes the transport of the substance in the microvasculature and must incorporate the potential difference existing there, i.e. free diffusion in a potential driven by perfusion, or what is usually called pseudo-diffusion, namely,

$$\langle \Gamma(t)\Gamma(t') \rangle = 2P\delta(t - t') \tag{47}$$

Equation 47 describes the second moment of a Gaussian distribution resulting from the spread of a δ function due to perfusion P. Equation 46 can be expressed in units of concentration $c(t)$ because the number of tracer molecules is conserved. Thus, all labelled spins are in the volume V (except those relaxing according to T_1), and this yields the following stochastic differential equation:

$$\frac{\partial c(V,t)}{\partial t} = -\frac{\partial}{\partial V}(F(V)c(V,t) + \Gamma(t)c(V,t) - \frac{c(V,t)}{T_1} \quad [48]$$

Equation 48 was rewritten to the Fokker-Planck equation and then solved for the conditions of the bolus-tracking experiment. In the original paper by Kelly et al. (147), the model was applied to a CASL experiment, where the input function is a constant during time *t*. In Paper III, the input function was adapted to PASL to fit our experimental settings, i.e. $c_{in} = c_0 \cdot e^{-\frac{t}{T_{1b}}}$, which implies

$$c(V,t) = \frac{C_0 \cdot e^{-\frac{t}{T_{1b}}}}{2} e^{\frac{TTT}{2 \cdot CTT}} \left(erfc\left(\frac{TTT}{\sqrt{4 \cdot CTT \cdot t}} - \sqrt{\left(\frac{1}{4 \cdot CTT} + \frac{1}{T_1}\right) t}\right) \times e^{\left(-\frac{TTT}{\sqrt{CTT}}\sqrt{\frac{1}{4 \cdot CTT} + \frac{1}{T_1}}\right)} \right) \Bigg|_{t=t-BL}^{t=t} \quad [49]$$

where TTT is the total transit time, which in statistical terms is the average time for blood plasma to traverse the entire system from the labelling plane to the imaging plane. TTT is the sum of the CTT and the ATT. ATT is the time for labelled blood to flow from the labelling region to the microvascular compartment of the imaging slice, and CTT is the time for intravascular water to distribute through the capillary bed by pseudo-diffusion and into the brain tissue by exchange through the BBB. In Paper IV, the use of an experimentally measured input function was proposed, resulting in

$$C(t) = \frac{TTT \cdot s}{\sqrt{4\pi \cdot CTT}} \int_0^t C_a(\tau) \frac{e^{-\frac{t-\tau}{T1}}}{(t-\tau)^{3/2}} exp\left(-\frac{TTT-(t-\tau)}{\sqrt{4 \cdot CTT \cdot (t-\tau)}}\right)^2 d\tau \quad [50]$$

where *s* is a scaling factor that corrects proportional errors in the registration of AIF concentration, such as partial volume effects, M_0 differences and different T_2 in blood and tissue. As seen above, the motion of water in the microvascular space is described by the second moment of a Gaussian distribution affected by a potential. The second moment describes the width of the Gaussian distribution, which could also be affected by transit through the BBB and may potentially reflect its integrity. It may be of interest in this context to compare the CTT with previously reported estimates by techniques with similar scope (136,141,143), as reported in more detail in Paper III. For example, the parameter CTT may be connected with other physiological parameters by

$$CTT \propto T_{IC \rightarrow EC} = \frac{1}{k_{in}} \quad [51]$$

In what follows, $r_{IC \to EC}$ is a phenomenological exchange term with a corresponding characteristic time constant denoted by $T_{IC \to EC}$, which depends, in addition to diffusion, on the effective exchange rate k_{in} of water from the IC to the EC (148) and is defined as

$$r_{IC \to EC}(t) = e^{-k_{in}t} \text{ and } r_{IC \to EC}(t) = e^{-t/T_{IC \to EC}} \qquad [52]$$

In addition, the parameter k_{in} also depends on physiological factors, such as the permeability-surface area product PS for water and the CBV (136), namely,

$$k_{in} = \frac{PS}{CBV} \qquad [53]$$

However, instead of using the total CBV, it is recommended to use the partial capillary volume fraction V_c, i.e. the fraction of the total blood volume in which exchange occurs (approximately one-third of the volume of the microvasculature, i.e. in human brain, $V_c = 1.5\, ml/100g$) (133,149).

The parameter PS was derived as follows (150):

$$PS = -CBF \cdot \ln{(1 - E)} \qquad [54]$$

where *E* is the extraction fraction, defined as the fractional transcapillary extraction during one single passage through the capillary system, and may be expressed as

$$E = (C_a - C_v)/C_a \qquad [55]$$

where C_a and C_v are the concentrations at the arterial inlet and the venous outlet of the capillary, respectively (150).

The CTT should not be confused with K^{trans} measured by the DCE-MRI technique, which reflects the transfer of gadolinium contrast agent from blood plasma through the BBB into the tissue. Hence, K^{trans} is the transfer constant of the contrast agent in units of ml/min/100g (151). CTT is in units *s* and is the average transit time of the ASL labelled water molecules experiencing any type of diffusion, where transport through the BBB is only one of the parts that contribute to the transit time of the labelled water molecules.

6.3 ASL assessment of haemodynamics in a clinical setting

Paper III focuses on the measurement of the transfer time of blood water through the capillaries and the BBB, as an alternative or complementary way to characterise the haemodynamics of the system, i.e. beyond, for example, CBV, CBF, MTT and K^{trans}. In several cerebral diseases, the BBB is affected and permeability is increased. Hence, the primary objective of the study described in Paper III was to adopt a preclinically implemented quantitative ASL method (147) to a clinical environment with the aim of using it as biomarker for early diagnosis of such diseases. Unlike the original implementation of the model, the investigation reported in Paper III employed pulsed ASL to decrease SAR levels. Furthermore, 3D-GRASE readout was used instead of EPI to expedite the acquisition and to further decrease SAR and increase SNR. Data evaluation was carried out using the proposed model (Equation 49) in 14 healthy adults and the resulting mean values (with corresponding SDs) of ATT, TTT and CTT for both occipital cortex (OC) and insular cortex (ICx). A test–retest analysis was included to verify the repeatability of the method. The values of CTT and ATT differed significantly among the ROIs ($p < 0.0001$). Longer ATT values were observed in OC, whereas CTT was longer in ICx.

As neither the normal inter-individual variability of parameters nor the potential pathophysiological effects in patients were accessible from previous studies, it was difficult to estimate the required accuracy. Therefore, simulations were performed before the analysis of experimental data to predict the effects of noise on the model parameters and estimate SNR-related measurement accuracy. It was found that the higher SNR levels (approximately 85) associated with larger ROIs (above 300 pixels) provided more accurate values of CTT (CI[95%] of ±8.8%), whereas less accurate CTT values (CI[95%] of ±12.1 %) can be expected from the lower SNR levels (approximately 60) of smaller ROIs (below 140 pixels). However, it was concluded that the model can be adapted to a clinical setting, and the CTT measurements can be added to the arsenal of potentially valuable hemodynamic parameters.

6.4 ASL assessment of haemodynamics in a preclinical setting

The key objective of the investigation described in Paper IV was to provoke the hemodynamic status of the tissue and test whether the corresponding alterations in measured parameters could be distinguished by the ASL approach. As a means of hemodynamic challenge, a previously described method for artificially modifying RBC deformability (152) was selected owing to its specific effect of occluding the microvasculature. Blood viscosity in the microcirculation is affected by the mechanical characteristics or the deformability of RBCs, and rigid RBCs will increase blood viscosity, which will in turn cause resistance to the flow in small capillaries, resulting in a decrease in CBF (153-155). The effects on mean CTT have not previously been documented, but our initial hypothesis was that mean CTT was likely to be prolonged. The MRI experiments were performed using a 9.4T horizontal bore animal scanner. A FAIR ASL sequence was used, similar to the labelling scheme used in the clinical setting (Paper III), and readout was accomplished by a three-shot segmented spin-echo EPI approach. Data were acquired in a time series ranging from 300 ms to 3000 ms, with a temporal resolution of 300 ms. The experiments were designed to observe haemodynamic changes in each animal before injection (one baseline measurement) and over time after injections (five post-injection measurements). The injections consisted of healthy/normal RBCs in the control group and rigid RBCs (i.e. with reduced deformability) in the study group. The fundamental findings reported in Paper IV were that a general decline in CBF (relative to the normalised baseline CBF) was observed after injection of RBCs with reduced deformability (entire brain), and that the changes in relative CBF in the study group were significantly different from the corresponding changes in the control group. The relative CBF after RBC injection was generally lower in the study group, and the most pronounced differences between groups after injection were seen in the putamen and in the white matter (15–20 percentage points difference between groups). The potential clinical implication of this is that CBF measurements using ASL may provide valuable information about, for example, treatment efficiency in cardiovascular disease, such as diabetes mellitus (angiopathy, retinopathy, nephropathy) (156), myocardial infraction, hypertension, as well as cerebrovascular accidents (157). In Paper IV, a local measurement of the AIF was also proposed as a further development of the ASL approach, partly to avoid AIF dispersion effects in the large arteries, but more importantly because the labelling profile is rarely perfect, particularly on a preclinical scanner with shorter RF and gradient coils.

As explained above, CTT depends only on dispersion, diffusion or filtration of the labelled spins, and the idea of using RBCs with decreased deformability was to increase the spatial heterogeneity of capillary flow without affecting the flow in the large arteries. As mentioned above, blood behaves as an incompressible Newtonian fluid in large arteries, and the decreased deformability of RBCs should not affect the flow in these vessels. Hence, the use of RBCs with decreased deformability should serve as a validation that CTT reflects properties of and processes in the capillary system. When the AIF scaling factor s (*cf.* Equation 50) was included as a free parameter to be estimated, the model could not provide reliable CTT results. This may be due to overfitting that occurs when a model with an excessively large number of free parameters is fitted to data. However, when the scaling factor s was fixed to the mean value over all pre- and post-injection time points obtained from the original fitting procedure, CTT results became more reasonable when the fit was repeated with fewer free parameters. The injection of deformed RBCs induced a 25% relative increase in CTT for the entire slice when s was fixed.

6.5 Sources of error in estimates based on the non-compartment modelling procedure

The non-compartment models described in Papers III and IV are noise sensitive, as illustrated in Table 1, Table 2 and Figure 15 below. Simulated concentration curves are shown for different SNR levels ranging from 5 to ∞, and all simulation procedures were repeated 1000 times at each noise level. The fitting algorithm failed to return correct parameters for noisy data, particularly at SNR = 5 and SNR = 10, but both precision and trueness were reduced even at SNR = 40, which corresponds to the SNR in a ROI of approximately the size of the putamen. Hence, SNR = 40 in a ROI is still not entirely sufficient to obtain an accurate estimation, owing to the sensitivity of the model to noise. The noise in the measured data induces a bias (a systematic error) in the estimates, and this bias is considerable if the noise level is high. The bias is difficult to predict because it depends on the true values. In the example below, the bias is exemplified for two different combinations of CTT and ATT.

Table 1:
Mean, standard deviation (SD) and coefficient of variation (CV=SD/Mean) of the CTT estimate after fitting of simulated data at different SNR levels for true values of CTT = 600 ms and ATT = 100 ms.

SNR	Mean [ms]	SD [ms]	CV
∞	600	0.00	0.00
100	593	143	0.24
40	559	216	0.37
10	500	331	0.66
5	473	387	0.82

Table 2:
Mean, standard deviation and coefficient of variation (CV=SD/Mean) of the CTT estimate after fitting of simulated data at different SNR levels for true values of CTT = 800 ms, ATT = 600 ms

SNR	Mean [ms]	SD [ms]	CV
∞	800	0.00	0.00
100	844	248	0.29
40	996	580	0.58
10	$1.10 \cdot 10^3$	868	0.77
5	$1.08 \cdot 10^3$	941	0.87

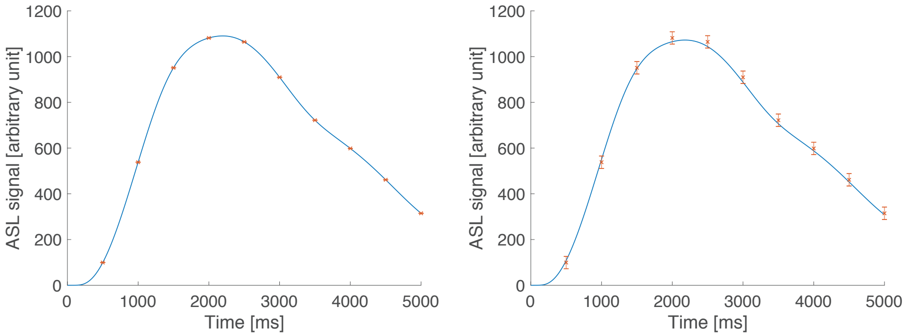

SNR = ∞ SNR = 40

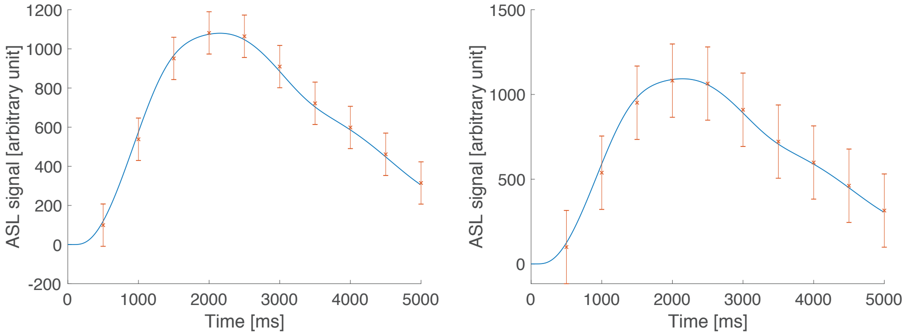

SNR = 10 SNR = 5

Figure 14:
Simulated dynamic arterial spin labelling (ASL) signal time courses (true values were CTT = 800 ms and ATT = 600 ms) for different SNRs. SNR (< ∞) was defined as the ratio of the maximal ASL signal in the dynamic time series to the noise standard deviation. The error bars reflect the noise standard deviations. All simulation procedures were repeated 1000 times. Model fits, using Equation 50, are shown as solid lines. The CTT and ATT estimates were 800 ms and 600 ms, respectively, for infinite SNR; 996 ms and 570 ms for SNR = 40; 1097 ms and 399 ms for SNR = 10, and 1078 ms and 398 ms for SNR = 5.

In the proposed derivations of the hemodynamic models, possible effects of arterial bolus dispersion have not been considered, as discussed in Paper III. The tracer bolus in the blood experiences friction against the vessel wall during its downstream travel through the vasculature, and this leads to a non-uniform velocity profile and, most likely, to dispersion. The cardiac pulsation is another factor in the blood flow variation in large arteries that also contributes to dispersion. The dispersion can be modelled as a convolution of $AIF(t)$ with the vascular transport function $VTF(t)$ (158), where the dispersed $AIF'(t)$ is given as

$$AIF'(t) = AIF(t) \otimes VTF(t) \qquad [56]$$

Two widely used VTFs are the Gaussian and gamma functions. The area under the curve for the VTF must be unity, as dispersion neither destroys nor creates label. The effects of dispersion in ASL have been modelled and examined, and it has been concluded that dispersion has a considerable effect on the ASL signal and thus causes systematic errors in the estimated CBF (118).

The CTT estimate reflects the diffusion component in the model, and dispersion, as can be seen in Equation 56, mimics the effects of diffusional motion and may interfere with the effects on the signal of pseudo-diffusion in capillaries and the filtration through BBB, thereby introducing a bias in the CTT estimates. However, in Paper IV a measured AIF (estimated closer to the tissue of interest) was proposed that could reduce such effects.

Furthermore, the model used in Papers III and IV is designed to provide estimates of the mean ATT and the mean CTT. ATT corresponds to the translational movement of the bolus, whereas CTT corresponds to the diffusion component (which is the sum of pseudo-diffusion in the capillary network and filtration through the BBB). However, when the signal is registered as a mean value from a ROI where different voxels within the ROI show different ATT, there is a risk that the model will capture the effects of this ATT distribution as a diffusion component, and in such a case, this would be reflected in the CTT estimate. This source of error is illustrated in Figures 15–16 below.

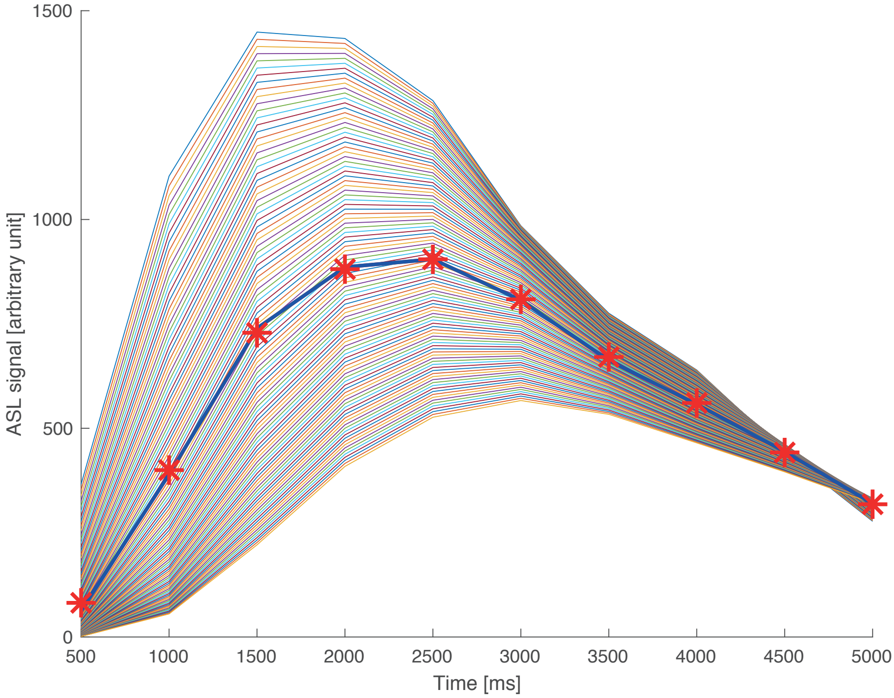

Figure 15:
Simulated, noise-free, dynamic arterial spin labelling (ASL) signal time courses, using Equation 50. The true CTT value was 800 ms and ATT ranged from from 0 ms to 2000 ms in steps of 20 ms. First, the mean value for each point in time was calculated. Thereafter, the model fit to the time curve consisting of the mean values (asterisks) was carried out, and the result of this fit is shown as a blue solid line. The estimated CTT and ATT values from the fit to the mean values were CTT = 2728 ms and ATT = 0 ms.

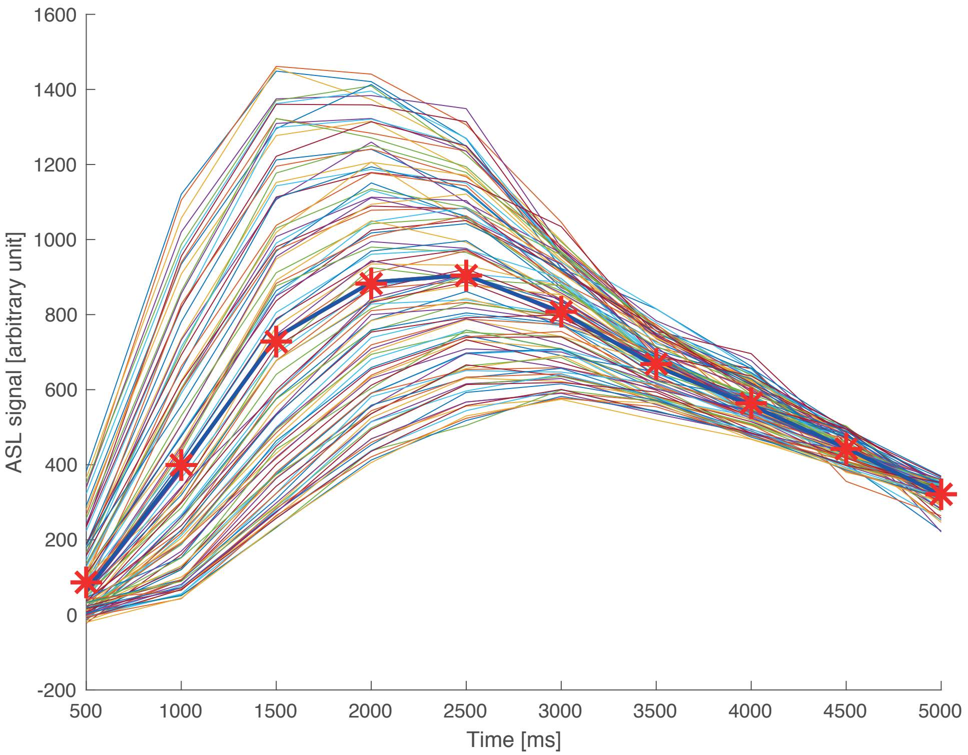

Figure 16:
Simulated (SNR = 40) dynamic arterial spin labelling (ASL) signal time courses using Equation 50. The true CTT value was 800 ms and ATT ranged from from 0 ms to 2000 ms in steps of 20 ms. First, the mean value for each point in time was calculated. Thereafter, the model fit to the time curve consisting of the mean values (asterisks) was carried out, and the result of this fit is shown as a blue solid line. The estimated CTT and ATT values from the fit to the mean values were CTT = 2731 ms and ATT = 0 ms. The results are based on 1000 repeated simulation with randomly added noise.

In the example in Figure 15, 200 concentration curves were simulated with the same CTT of 800 ms but different ATT, ranging from 0 to 2000 ms in steps of 20 ms. Noise was not added, but the algorithm seemed to interpret a distribution of ATT as an addition to the inherent CTT. The solid line represents the mean signal of all curves (which corresponds to the measured mean signal in a ROI). Fitting of the model (Equation 50) to the mean signal data resulted in an ATT estimate of 0 ms and a CTT estimate of 2728 ms. The example shown in Figure 16 represents the same situation, but at SNR = 40, and the conclusion was highly similar to the noise-free case.

Another limitation of the model is that the effects of venous outflow may violate the assumption that concentration is a conserved quantity, but this effect is likely to be small in the context of ASL owing to the small fraction of unextracted water (54) in combination with the longitudinal relaxation of the spins in the capillaries.

Chapter 7

Conclusions and future work

The scientific work presented in this doctoral thesis focused on MRI signal denoising and its effects on relevant diffusion and perfusion parameters and on the development of a non-compartment modelling approach for characterising the transport of vascular water.

In Paper I, it was concluded that the designed wavelet-domain filter is an attractive model-free approach for reducing noise effects (rectified noise floor as well as SD) in magnitude MR images for diffusion applications. The results from simulations as well as experiments illustrated the increased visual and quantitative usefulness of high-*b*-value DW images after denoising. Systematic noise-related errors in anisotropy indices appeared to be reduced by the proposed denoising scheme.

The study reported in Paper II, including both simulated and experimental data, showed that wavelet-domain filtering can be used to maintain perfusion quantification accuracy in ASL with a reduced number of averages, as well as to increase the visual image quality. Both wavelet-domain filtering and Gaussian smoothing corrupted to some extent the signal in areas close to borders. For the wavelet-domain filter, this effect decreased with higher SNR, whereas for Gaussian smoothing it remained the same independently of SNR. If time allows, the high quality of ASL-based CBF maps is always best accomplished by extending the number of averages, provided that the subject does not undergo any movement during the image acquisition. Denoising by post-processing is, however, an attractive way to maintain CBF precision and accuracy with a reduced number of averages, with potential usefulness also in dynamic applications such as ASL-fMRI and model-free ASL techniques.

The 4D imaging approach in modern MRI applications (i.e. three spatial and one temporal or b-value-dimension) is becoming increasingly common. Hence, it would be reasonable for future studies to focus on adapting similar filters as those presented in Paper I and Paper II to 4D data, where the filtering algorithm considers all volumes at the same time. Handling such 4D datasets is computationally demanding, and thus implementing the filtering algorithms on the graphics processing unit (GPU) would be an attractive alternative. The increasing number of medical images accumulating in large medical image databases also opens opportunities to use machine learning (ML) for denoising (159). Advances in ML-based denoising algorithms will most likely be driven by the development of new ML techniques for diagnosis, detection and prediction of diseases.

Paper III focuses on the measurement of the transfer time of the blood water through capillaries into the extravascular space, referred to as CTT, as well as the water transport in large arteries from the labelling site to the arterioles, where the blood flow is laminar, referred to as ATT. The parameters were obtained by an adaption of a previously proposed preclinical model that was applied to a small-bore MRI scanner using a CASL technique (112), to a human MRI environment using a more clinically appropriate PASL technique. The study indicated that the noise induces a bias in the resulting estimates, and that high SNR (> 100) is required for highly accurate results.

The primary aim of Paper IV was to alter the hemodynamics in experimental animals by controlled manipulation of the flow in the microvasculature, and to test whether ASL measurements are sufficiently robust and sensitive to capture the corresponding alterations in CBF and CTT. The hemodynamic challenge was accomplished by injection of RBCs with decreased deformability into the microvasculature, resulting in a slower RBC flow (160,161), which was hypothesised to influence the CTT. With regard to CBF, the study indicated that the ASL measurements could detect CBF changes caused by injection of RBCs with mildly reduced deformability relative to a control group in which normal RBCs were injected. If the scaling factor s (*cf.* Equation 50) was fixed to a reasonable value, the CTT in the study group generally increased after injection, with a difference relative to the control group that corresponded to approximately 15–40 percentage points. The study seems to confirm that there is a correlation between mildly reduced RBC deformability and decreased CBF, and promising ASL results with regard to the potential of observing changes in capillary water transfer times were also obtained.

The CTT measured by the technique presented in Papers III and IV is, however, still in need of a systematic investigation. It would be of value to ensure that the model can in fact provide a reasonable and robust measure of the transfer of water molecules in the microvasculature, reflecting only the pseudo-diffusion and the filtration across the BBB. Therefore, it is necessary to continue to improve SNR so that the method can be thoroughly investigated. As an alternative to the damaged RBCs, another validation approach would be to disrupt the BBB, for example, by mannitol injection (162) or by using ultrasound (163), which should influence the transfer time across the BBB.

Acknowledgements

First of all, I would like to thank my main supervisor Professor Ronnie Wirestam, who always found time for guidance and discussion. Without his intellectual contribution, not a single word in this thesis would have been written. I have really been very fortunate to have him as my supervisor.

I would also like to thank to my co-supervisors Professor Linda Knutsson and Professor Freddy Ståhlberg for helping in the design of all experiments, guidance, support and editing assistance.

I am grateful to all co-authors of the papers in this thesis, particular Professor Jonas Åkeson and Dr. Anders Schmidt for providing the image data used in Paper III, and Dr. Matthias Günther for providing the ASL pulse sequence and quantification tool. Of course, I am grateful to all co-authors for editing assistance.

Special thanks for friendship and help go to all my colleagues at the Department of Medical Radiation Physics in general and, in particular, all past and present members of the MR physics group in Lund: Sara Brockstedt, Jimmy Lätt, Peter Mannfolk, Karin Markenroth Bloch, Markus Nilsson, Johan Olsrud, Tea Sordia, Renata Madru, Johanna Mårtensson, Anders Nilsson, Anna Rydhög, Emelie Lind, André Ahlgren, Filip Szczepankiewicz, Mads Andersen, Gunther Helms, Pernilla Peterson, Olof Strandberg, Jonas Svensson, Frederik Testud, Björn Lampinen, Anna Lundberg, Hampus Olsson, Johanna Arborelius, Boel Hansson, Titti Owman, Vladimir Denisov, Carina Siversson, René in't Zandt, Michael Gottschalk and others.

Finally, I would like to thank my family and friends for their support, patience and understanding.

This work was financially supported by the Swedish Research Council (grant numbers 13514, 2005-6910, 2007-3975, 2007-6079, 2010-4454 and 2017-00995), K&A Wallenberg foundation (grant no. 1998.0182), the Crafoord Foundation and the Swedish Cancer Foundation (grant numbers CAN 2009/176, CAN 2012/597 and CAN 2015/567).

References

1. Assaf Y, Pasternak O. Diffusion tensor imaging (DTI)-based white matter mapping in brain research: A review. Journal of Molecular Neuroscience 2008;34(1):51-61.
2. Calamante F, Thomas DL, Pell GS, Wiersma J, Turner R. Measuring cerebral blood flow using magnetic resonance imaging techniques. J Cereb Blood Flow Metab 1999;19(7):701-735.
3. Sorensen AG, Buonanno FS, Gonzalez RG, Schwamm LH, Lev MH, Huang-Hellinger FR, Reese TG, Weisskoff RM, Davis TL, Suwanwela N, Can U, Moreira JA, Copen WA, Look RB, Finklestein SP, Rosen BR, Koroshetz WJ. Hyperacute stroke: evaluation with combined multisection diffusion-weighted and hemodynamically weighted echo-planar MR imaging. Radiology 1996;199(2):391-401.
4. Fisher M, Albers GW. Applications of diffusion-perfusion magnetic resonance imaging in acute ischemic stroke. Neurology 1999;52(9):1750-1756.
5. Fisher M, Ginsberg M. Current concepts of the ischemic penumbra - Introduction. Stroke 2004;35(11):2657-2658.
6. Ma H, Zavala JA, Teoh H, Churilov L, Gunawan M, Ly J, Wright P, Phan T, Arakawa S, Davis SM, Donnan GA. Penumbral mismatch is underestimated using standard volumetric methods and this is exacerbated with time. Journal of Neurology Neurosurgery and Psychiatry 2009;80(9):991-996.
7. Warach S. Measurement of the ischemic penumbra with MRI: it's about time. Stroke 2003;34(10):2533-2534.
8. Schellinger PD, Bryan RN, Caplan LR, Detre JA, Edelman RR, Jaigobin C, Kidwell CS, Mohr JP, Sloan M, Sorensen AG, Warach S, Therapeutics, Technology Assessment Subcommittee of the American Academy of N. Evidence-based guideline: The role of diffusion and perfusion MRI for the diagnosis of acute ischemic stroke: report of the Therapeutics and Technology Assessment Subcommittee of the American Academy of Neurology. Neurology 2010;75(2):177-185.
9. Kidwell CS, Chalela JA, Saver JL, Starkman S, Hill MD, Demchuk AM, Butman JA, Patronas N, Alger JR, Latour LL, Luby ML, Baird AE, Leary MC, Tremwel M, Ovbiagele B, Fredieu A, Suzuki S, Villablanca JP, Davis S, Dunn B, Todd JW, Ezzeddine MA, Haymore J, Lynch JK, Davis L, Warach S. Comparison of MRI and CT for detection of acute intracerebral hemorrhage. JAMA 2004;292(15):1823-1830.

10. Fiebach JB, Schellinger PD, Gass A, Kucinski T, Siebler M, Villringer A, Olkers P, Hirsch JG, Heiland S, Wilde P, Jansen O, Rother J, Hacke W, Sartor K, B5 KS. Stroke magnetic resonance imaging is accurate in hyperacute intracerebral hemorrhage - A multicenter study on the validity of stroke imaging. Stroke 2004;35(2):502-506.
11. Provenzale JM, Mukundan S, Barboriak DP. Diffusion-weighted and perfusion MR imaging for brain tumor characterization and assessment of treatment response. Radiology 2006;239(3):632-649.
12. Daldrup-Link HE, Brasch RC. Macromolecular contrast agents for MR mammography: current status. European Radiology 2003;13(2):354-365.
13. Yang S, Law M, Zagzag D, Wu HH, Cha SM, Golfinos JG, Knopp EA, Johnson G. Dynamic contrast-enhanced perfusion MR imaging measurements of endothelial permeability: Differentiation between atypical and typical meningiomas. American Journal of Neuroradiology 2003;24(8):1554-1559.
14. Desjardins A, Barboriak D, Herndon JE, Reardon D, Quinn J, Rich J, Sathornsumetee S, Friedman H, Vredenburgh J. Evaluation of tumor response by dynamic contrast-enhanced magnetic resonance imaging in glioblastoma (gbm) patients treated with bevacizumab (bev) and irinotecan (CPT-11). Neuro-Oncology 2007;9(4):573-574.
15. Jones DK, Basser PJ. "Squashing peanuts and smashing pumpkins": how noise distorts diffusion-weighted MR data. Magn Reson Med 2004;52(5):979-993.
16. Baliyan V, Das CJ, Sharma R, Gupta AK. Diffusion weighted imaging: Technique and applications. World J Radiol 2016;8(9):785-798.
17. Silva MD, Omae T, Helmer KG, Li F, Fisher M, Sotak CH. Separating changes in the intra- and extracellular water apparent diffusion coefficient following focal cerebral ischemia in the rat brain. Magn Reson Med 2002;48(5):826-837.
18. Koh DM, Collins DJ. Diffusion-weighted MRI in the body: applications and challenges in oncology. AJR Am J Roentgenol 2007;188(6):1622-1635.
19. Fan G, Zang P, Jing F, Wu Z, Guo Q. Usefulness of diffusion/perfusion-weighted MRI in rat gliomas: correlation with histopathology. Acad Radiol 2005;12(5):640-651.
20. Hochmuth RM, Waugh RE. Erythrocyte-Membrane Elasticity and Viscosity. Annual Review of Physiology 1987;49:209-219.
21. Lichtman MA, Heal J, Rowe JM. Hyperleukocytic leukaemia: rheological and clinical features and management. Baillieres Clin Haematol 1987;1(3):725-746.

22. Pries AR, Secomb TW, Gaehtgens P. Biophysical aspects of blood flow in the microvasculature. Cardiovascular Research 1996;32(4):654-667.
23. Bayliss LE. The Axial Drift of the Red Cells When Blood Flows in a Narrow Tube. Journal of Physiology-London 1959;149(3):593-613.
24. Fahraeus R. The suspension stability of the blood. Physiological Reviews 1929;9(2):241-274.
25. van Zijl PC, Eleff SM, Ulatowski JA, Oja JM, Ulug AM, Traystman RJ, Kauppinen RA. Quantitative assessment of blood flow, blood volume and blood oxygenation effects in functional magnetic resonance imaging. Nat Med 1998;4(2):159-167.
26. Meier P, Zierler KL. On the theory of the indicator-dilution method for measurement of blood flow and volume. J Appl Physiol 1954;6(12):731-744.
27. Weisskoff RM, Chesler D, Boxerman JL, Rosen BR. Pitfalls in MR measurement of tissue blood flow with intravascular tracers: which mean transit time? Magn Reson Med 1993;29(4):553-558.
28. Leenders KL, Perani D, Lammertsma AA, Heather JD, Buckingham P, Healy MJ, Gibbs JM, Wise RJ, Hatazawa J, Herold S, et al. Cerebral blood flow, blood volume and oxygen utilization. Normal values and effect of age. Brain 1990;113 (Pt 1):27-47.
29. Melamed E, Lavy S, Bentin S, Cooper G, Rinot Y. Reduction in regional cerebral blood flow during normal aging in man. Stroke 1980;11(1):31-35.
30. Gur RC, Gur RE, Obrist WD, Skolnick BE, Reivich M. Age and Regional Cerebral Blood-Flow at Rest and during Cognitive Activity. Archives of General Psychiatry 1987;44(7):617-621.
31. Meltzer CC, Cantwell MN, Greer PJ, Ben-Eliezer D, Smith G, Frank G, Kaye WH, Houck PR, Price JC. Does cerebral blood flow decline in healthy aging? A PET study with partial-volume correction. Journal of Nuclear Medicine 2000;41(11):1842-1848.
32. Todd NV, Picozzi P, Crockard HA. Quantitative measurement of cerebral blood flow and cerebral blood volume after cerebral ischaemia. J Cereb Blood Flow Metab 1986;6(3):338-341.
33. Drabek T, Foley LM, Janata A, Stezoski J, Hitchens K, Manole MD, Kochanek PM. Global and regional differences in cerebral blood flow after asphyxial versus ventricular fibrillation cardiac arrest in rats using ASL-MRI. Resuscitation 2014;85(7):964-971.
34. Shaul ME, Hallacoglu B, Sassaroli A, Shukitt-Hale B, Fantini S, Rosenberg IH, Troen AM. Cerebral blood volume and vasodilation are independently diminished by aging and hypertension: a near infrared spectroscopy study. J Alzheimers Dis 2014;42 Suppl 3:S189-198.

35. Calamante F, Thomas DL, Pell GS, Wiersma J, Turner R. Measuring cerebral blood flow using magnetic resonance imaging techniques. Journal of Cerebral Blood Flow and Metabolism 1999;19(7):701-735.
36. Horitsugi G, Watabe T, Kanai Y, Ikeda H, Kato H, Naka S, Ishibashi M, Matsunaga K, Isohashi K, Shimosegawa E, Hatazawa J. Oxygen-15 labeled CO2, O-2, and CO PET in small animals: evaluation using a 3D-mode microPET scanner and impact of reconstruction algorithms. Ejnmmi Research 2017;7.
37. Forbes ML, Hendrich KS, Kochanek PM, Williams DS, Schiding JK, Wisniewski SR, Kelsey SF, DeKosky ST, Graham SH, Marion DW, Ho C. Assessment of cerebral blood flow and CO2 reactivity after controlled cortical impact by perfusion magnetic resonance imaging using arterial spin-labeling in rats. Journal of Cerebral Blood Flow and Metabolism 1997;17(8):865-874.
38. Cremer JE, Seville MP. Regional brain blood flow, blood volume, and haematocrit values in the adult rat. J Cereb Blood Flow Metab 1983;3(2):254-256.
39. Grubb RL, Jr., Raichle ME, Eichling JO, Ter-Pogossian MM. The effects of changes in PaCO2 on cerebral blood volume, blood flow, and vascular mean transit time. Stroke 1974;5(5):630-639.
40. Cottrell GT, Ferguson AV. Sensory circumventricular organs: central roles in integrated autonomic regulation. Regulatory Peptides 2004;117(1):11-23.
41. Eichling JO, Raichle ME, Grubb RL, Jr., Ter-Pogossian MM. Evidence of the limitations of water as a freely diffusible tracer in brain of the rhesus monkey. Circ Res 1974;35(3):358-364.
42. Brown R. A brief account of microscopical observations made in the months of June, July and August, 1827, on the particles contained in the pollen of plants; and on the general existence of active molecules in organic and inorganic bodies. Philosophical Magazine 1828;4:161-173.
43. Li TC, Kheifets S, Medellin D, Raizen MG. Measurement of the Instantaneous Velocity of a Brownian Particle. Science 2010;328(5986):1673-1675.
44. Einstein A. Theoretical remarks on the Brownian Motion. Zeitschrift Fur Elektrochemie Und Angewandte Physikalische Chemie 1907;13:41-42.
45. Le Bihan D, Mangin JF, Poupon C, Clark CA, Pappata S, Molko N, Chabriat H. Diffusion tensor imaging: concepts and applications. J Magn Reson Imaging 2001;13(4):534-546.

46. Stejskal EO, Tanner JE. Spin Diffusion Measurements: Spin Echoes in the Presence of a Time-Dependent Field Gradient. Journal of Chemical Physics 1965;42(1):288-+.
47. Basser PJ, Pierpaoli C. Microstructural and physiological features of tissues elucidated by quantitative-diffusion-tensor MRI. J Magn Reson B 1996;111(3):209-219.
48. Mori S, van Zijl PC. Fiber tracking: principles and strategies - a technical review. NMR Biomed 2002;15(7-8):468-480.
49. Liu C, Bammer R, Moseley ME. Limitations of apparent diffusion coefficient-based models in characterizing non-gaussian diffusion. Magn Reson Med 2005;54(2):419-428.
50. Jensen JH, Helpern JA, Ramani A, Lu H, Kaczynski K. Diffusional kurtosis imaging: the quantification of non-gaussian water diffusion by means of magnetic resonance imaging. Magn Reson Med 2005;53(6):1432-1440.
51. Tabesh A, Jensen JH, Ardekani BA, Helpern JA. Estimation of tensors and tensor-derived measures in diffusional kurtosis imaging. Magn Reson Med 2011;65(3):823-836.
52. Ginsberg MD, Busto R, Harik SI. Regional blood-brain barrier permeability to water and cerebral blood flow during status epilepticus: insensitivity to norepinephrine depletion. Brain Res 1985;337(1):59-71.
53. Silva AC, Williams DS, Koretsky AP. Evidence for the exchange of arterial spin-labeled water with tissue water in rat brain from diffusion-sensitized measurements of perfusion. Magn Reson Med 1997;38(2):232-237.
54. Herscovitch P, Raichle ME, Kilbourn MR, Welch MJ. Positron Emission Tomographic Measurement of Cerebral Blood-Flow and Permeability Surface-Area Product of Water Using [O-15]Water and [C-11] Butanol. Journal of Cerebral Blood Flow and Metabolism 1987;7(5):527-542.
55. Detre JA, Leigh JS, Williams DS, Koretsky AP. Perfusion imaging. Magn Reson Med 1992;23(1):37-45.
56. Williams DS, Detre JA, Leigh JS, Koretsky AP. Magnetic resonance imaging of perfusion using spin inversion of arterial water. Proceedings of the National Academy of Sciences of the United States of America 1992;89(1):212-216.
57. Zhang W, Silva AC, Williams DS, Koretsky AP. NMR measurement of perfusion using arterial spin labeling without saturation of macromolecular spins. Magn Reson Med 1995;33(3):370-376.

58. Edelman RR, Siewert B, Darby DG, Thangaraj V, Nobre AC, Mesulam MM, Warach S. Qualitative mapping of cerebral blood flow and functional localization with echo-planar MR imaging and signal targeting with alternating radio frequency. Radiology 1994;192(2):513-520.
59. Kwong KK, Chesler DA, Weisskoff RM, Donahue KM, Davis TL, Ostergaard L, Campbell TA, Rosen BR. MR perfusion studies with T1-weighted echo planar imaging. Magn Reson Med 1995;34(6):878-887.
60. Gunther M, Oshio K, Feinberg DA. Single-shot 3D imaging techniques improve arterial spin labeling perfusion measurements. Magn Reson Med 2005;54(2):491-498.
61. van Osch MJ, Teeuwisse WM, Chen Z, Suzuki Y, Helle M, Schmid S. Advances in arterial spin labelling MRI methods for measuring perfusion and collateral flow. J Cereb Blood Flow Metab 2018;38(9):1461-1480.
62. Dai WY, Garcia D, de Bazelaire C, Alsop DC. Continuous Flow-Driven Inversion for Arterial Spin Labeling Using Pulsed Radio Frequency and Gradient Fields. Magn Reson Imaging 2008;60(6):1488-1497.
63. Heijtel DF, Mutsaerts HJ, Bakker E, Schober P, Stevens MF, Petersen ET, van Berckel BN, Majoie CB, Booij J, van Osch MJ, Vanbavel E, Boellaard R, Lammertsma AA, Nederveen AJ. Accuracy and precision of pseudo-continuous arterial spin labeling perfusion during baseline and hypercapnia: a head-to-head comparison with (1)(5)O H(2)O positron emission tomography. Neuroimage 2014;92:182-192.
64. Zhang K, Herzog H, Mauler J, Filss C, Okell TW, Kops ER, Tellmann L, Fischer T, Brocke B, Sturm W, Coenen HH, Shah NJ. Comparison of cerebral blood flow acquired by simultaneous [15O]water positron emission tomography and arterial spin labeling magnetic resonance imaging. J Cereb Blood Flow Metab 2014;34(8):1373-1380.
65. Kilroy E, Apostolova L, Liu C, Yan L, Ringman J, Wang DJ. Reliability of two-dimensional and three-dimensional pseudo-continuous arterial spin labeling perfusion MRI in elderly populations: comparison with 15O-water positron emission tomography. J Magn Reson Imaging 2014;39(4):931-939.
66. Wong EC, Cronin M, Wu WC, Inglis B, Frank LR, Liu TT. Velocity-selective arterial spin labeling. Magn Reson Med 2006;55(6):1334-1341.
67. Wong WHE, Maller JJ. Arterial Spin Labeling Techniques 2009-2014. Journal of Medical Imaging and Radiation Sciences 2016;47(1):98-107.

68. Wong EC. New developments in arterial spin labeling pulse sequences. NMR Biomed 2013;26(8):887-891.
69. Qin Q, van Zijl PC. Velocity-selective-inversion prepared arterial spin labeling. Magn Reson Med 2016;76(4):1136-1148.
70. Buxton RB, Frank LR, Wong EC, Siewert B, Warach S, Edelman RR. A general kinetic model for quantitative perfusion imaging with arterial spin labeling. Magn Reson Med 1998;40(3):383-396.
71. Kety SS. The Theory and Applications of the Exchange of Inert Gas at the Lungs and Tissues. Pharmacological Reviews 1951;3(1):1-41.
72. Herscovitch P, Raichle ME. What Is the Correct Value for the Brain Blood Partition-Coefficient for Water. Journal of Cerebral Blood Flow and Metabolism 1985;5(1):65-69.
73. Henkelman RM. Measurement of signal intensities in the presence of noise in MR images. Med Phys 1985;12(2):232-233.
74. Gudbjartsson H, Patz S. The Rician distribution of noisy MRI data. Magn Reson Med 1995;34(6):910-914.
75. Koay CG, Basser PJ. Analytically exact correction scheme for signal extraction from noisy magnitude MR signals. J Magn Reson 2006;179(2):317-322.
76. Aja-Fernandez S, Alberola-Lopez C, Westin CF. Noise and signal estimation in magnitude MRI and Rician distributed images: a LMMSE approach. IEEE Trans Image Process 2008;17(8):1383-1398.
77. Papoulis A. The Fourier Integral and its Applications. McGraw-Hill Co, New York 1962.
78. Dietrich O, Raya JG, Reeder SB, Ingrisch M, Reiser MF, Schoenberg SO. Influence of multichannel combination, parallel imaging and other reconstruction techniques on MRI noise characteristics. Magn Reson Imaging 2008;26(6):754-762.
79. Pruessmann KP, Weiger M, Scheidegger MB, Boesiger P. SENSE: sensitivity encoding for fast MRI. Magn Reson Med 1999;42(5):952-962.
80. Griswold MA, Jakob PM, Heidemann RM, Nittka M, Jellus V, Wang J, Kiefer B, Haase A. Generalized autocalibrating partially parallel acquisitions (GRAPPA). Magn Reson Med 2002;47(6):1202-1210.
81. Thunberg P, Zetterberg P. Noise distribution in SENSE- and GRAPPA-reconstructed images: a computer simulation study. Magn Reson Imaging 2007;25(7):1089-1094.
82. Kruger G, Glover GH. Physiological noise in oxygenation-sensitive magnetic resonance imaging. Magn Reson Med 2001;46(4):631-637.
83. Basser PJ, Mattiello J, LeBihan D. MR diffusion tensor spectroscopy and imaging. Biophys J 1994;66(1):259-267.

84. King MD, Houseman J, Roussel SA, van Bruggen N, Williams SR, Gadian DG. q-Space imaging of the brain. Magn Reson Med 1994;32(6):707-713.
85. Tuch DS, Reese TG, Wiegell MR, Makris N, Belliveau JW, Wedeen VJ. High angular resolution diffusion imaging reveals intravoxel white matter fiber heterogeneity. Magnetic Resonance in Medicine 2002;48(4):577-582.
86. Ozarslan E, Koay CG, Shepherd TM, Komlosh ME, Irfanoglu MO, Pierpaoli C, Basser PJ. Mean apparent propagator (MAP) MRI: a novel diffusion imaging method for mapping tissue microstructure. Neuroimage 2013;78:16-32.
87. Zhang H, Schneider T, Wheeler-Kingshott CA, Alexander DC. NODDI: practical in vivo neurite orientation dispersion and density imaging of the human brain. Neuroimage 2012;61(4):1000-1016.
88. Le Bihan D, Poupon C, Amadon A, Lethimonnier F. Artifacts and pitfalls in diffusion MRI. J Magn Reson Imaging 2006;24(3):478-488.
89. Clark CA, Le Bihan D. Water diffusion compartmentation and anisotropy at high b values in the human brain. Magn Reson Med 2000;44(6):852-859.
90. Anderson AW. Theoretical analysis of the effects of noise on diffusion tensor imaging. Magn Reson Med 2001;46(6):1174-1188.
91. Wong EC, Buxton RB, Frank LR. A theoretical and experimental comparison of continuous and pulsed arterial spin labeling techniques for quantitative perfusion imaging. Magn Reson Med 1998;40(3):348-355.
92. Wong EC, Buxton RB, Frank LR. Quantitative imaging of perfusion using a single subtraction (QUIPSS and QUIPSS II). Magnetic Resonance in Medicine 1998;39(5):702-708.
93. Luh WM, Wong EC, Bandettini PA, Hyde JS. QUIPSS II with thin-slice TI1 periodic saturation: a method for improving accuracy of quantitative perfusion imaging using pulsed arterial spin labeling. Magn Reson Med 1999;41(6):1246-1254.
94. Wink AM, Roerdink JB. BOLD Noise Assumptions in fMRI. Int J Biomed Imaging 2006;2006:12014.
95. Wong EC, Buxton RB, Frank LR. Implementation of quantitative perfusion imaging techniques for functional brain mapping using pulsed arterial spin labeling. NMR Biomed 1997;10(4-5):237-249.
96. Aguirre GK, Detre JA, Zarahn E, Alsop DC. Experimental design and the relative sensitivity of BOLD and perfusion fMRI. Neuroimage 2002;15(3):488-500.

97. Murase K, Yamazaki Y, Shinohara M, Kawakami K, Kikuchi K, Miki H, Mochizuki T, Ikezoe J. An anisotropic diffusion method for denoising dynamic susceptibility contrast-enhanced magnetic resonance images. Phys Med Biol 2001;46(10):2713-2723.
98. Healy DM, Weaver JB. 2 Applications of Wavelet Transforms in Magnetic-Resonance-Imaging. Ieee Transactions on Information Theory 1992;38(2):840-860.
99. Weaver JB, Xu YS, Healy DM, Cromwell LD. Filtering Noise from Images with Wavelet Transforms. Magnetic Resonance in Medicine 1991;21(2):288-295.
100. Donoho DL. De-Noising by Soft-Thresholding. Ieee Transactions on Information Theory 1995;41(3):613-627.
101. Chipman HA, Kolaczyk ED, McCullogh RE. Adaptive Bayesian wavelet shrinkage. Journal of the American Statistical Association 1997;92(440):1413-1421.
102. Nowak RD. Wavelet-based Rician noise removal for magnetic resonance imaging. IEEE Trans Image Process 1999;8(10):1408-1419.
103. Wink AM, Roerdink JB. Denoising functional MR images: a comparison of wavelet denoising and Gaussian smoothing. IEEE Trans Med Imaging 2004;23(3):374-387.
104. Wirestam R, Stahlberg F. Wavelet-based noise reduction for improved deconvolution of time-series data in dynamic susceptibility-contrast MRI. MAGMA 2005;18(3):113-118.
105. McKeown MJ, Hansen LK, Sejnowski TJ. Independent component analysis of functional MRI: what is signal and what is noise? Current Opinion in Neurobiology 2003;13(5):620-629.
106. Ghael SP, Sayeed AM, Baraniuk RG. Improved wavelet denoising via empirical Wiener filtering. Wavelet Applications in Signal and Image Processing V 1997;3169:389-399.
107. Starck JL, Candes EJ, Donoho DL. The curvelet transform for image denoising. IEEE Trans Image Process 2002;11(6):670-684.
108. Do MN, Vetterli M. The contourlet transform: an efficient directional multiresolution image representation. IEEE Trans Image Process 2005;14(12):2091-2106.
109. Ding Z, Gore JC, Anderson AW. Reduction of noise in diffusion tensor images using anisotropic smoothing. Magn Reson Med 2005;53(2):485-490.
110. Arfanakis K, Cordes D, Haughton VM, Carew JD, Meyerand ME. Independent component analysis applied to diffusion tensor MRI. Magn Reson Med 2002;47(2):354-363.

111. Parker GJ, Schnabel JA, Symms MR, Werring DJ, Barker GJ. Nonlinear smoothing for reduction of systematic and random errors in diffusion tensor imaging. J Magn Reson Imaging 2000;11(6):702-710.
112. Zaroubi S, Goelman G. Complex denoising of MR data via wavelet analysis: Application for functional MRI. Magn Reson Imaging 2000;18(1):59-68.
113. Mulkern RV, Vajapeyam S, Haker SJ, Maier SE. Magnetization transfer studies of the fast and slow tissue water diffusion components in the human brain. NMR Biomed 2005;18(3):186-194.
114. Hutchinson EB, Avram AV, Irfanoglu MO, Koay CG, Barnett AS, Komlosh ME, Ozarslan E, Schwerin SC, Juliano SL, Pierpaoli C. Analysis of the Effects of Noise, DWI Sampling, and Value of Assumed Parameters in Diffusion MRI Models. Magn Reson Med 2017;78(5):1767-1780.
115. Alexander DC, Hubbard PL, Hall MG, Moore EA, Ptito M, Parker GJ, Dyrby TB. Orientationally invariant indices of axon diameter and density from diffusion MRI. Neuroimage 2010;52(4):1374-1389.
116. Aja-Fernandez S, Tristan-Vega A, Alberola-Lopez C. Noise estimation in single- and multiple-coil magnetic resonance data based on statistical models. Magn Reson Imaging 2009;27(10):1397-1409.
117. Lim YM, Cho YW, Shamim S, Solomon J, Birn R, Luh WM, Gaillard WD, Ritzl EK, Theodore WH. Usefulness of pulsed arterial spin labeling MR imaging in mesial temporal lobe epilepsy. Epilepsy Res 2008;82(2-3):183-189.
118. Wu WC, Mazaheri Y, Wong EC. The effects of flow dispersion and cardiac pulsation in arterial spin labeling. IEEE Trans Med Imaging 2007;26(1):84-92.
119. Noth U, Meadows GE, Kotajima F, Deichmann R, Corfield DR, Turner R. Cerebral vascular response to hypercapnia: determination with perfusion MRI at 1.5 and 3.0 Tesla using a pulsed arterial spin labeling technique. J Magn Reson Imaging 2006;24(6):1229-1235.
120. Petersen ET, Zimine I, Ho YCL, Golay X. Non-invasive measurement of perfusion: a critical review of arterial spin labelling techniques. British Journal of Radiology 2006;79(944):688-701.
121. Tsekos NV, Zhang FY, Merkle H, Nagayama M, Iadecola C, Kim SG. Quantitative measurements of cerebral blood flow in rats using the FAIR technique: Correlation with previous iodoantipyrine autoradiographic studies. Magnetic Resonance in Medicine 1998;39(4):564-573.

122. Ferre JC, Petr J, Bannier E, Barillot C, Gauvrit JY. Improving quality of arterial spin labeling MR imaging at 3 tesla with a 32-channel coil and parallel imaging. J Magn Reson Imaging 2012;35(5):1233-1239.
123. Ye FQ, Frank JA, Weinberger DR, McLaughlin AC. Noise reduction in 3D perfusion imaging by attenuating the static signal in arterial spin tagging (ASSIST). Magnetic Resonance in Medicine 2000;44(1):92-100.
124. Wong EC, Luh WM, Liu TT. Turbo ASL: Arterial spin labeling with higher SNR and temporal resolution. Magnetic Resonance in Medicine 2000;44(4):511-515.
125. Jahanian H, Noll DC, Hernandez-Garcia L. B0 field inhomogeneity considerations in pseudo-continuous arterial spin labeling (pCASL): effects on tagging efficiency and correction strategy. NMR Biomed 2011;24(10):1202-1209.
126. Restom K, Behzadi Y, Liu TT. Physiological noise reduction for arterial spin labeling functional MRI. Neuroimage 2006;31(3):1104-1115.
127. Behzadi Y, Restom K, Liau J, Liu TT. A component based noise correction method (CompCor) for BOLD and perfusion based fMRI. Neuroimage 2007;37(1):90-101.
128. Wang JJ, Wang Z, Aguirre GK, Detre JA. To smooth or not to smooth? - ROC analysis of perfusion fMRI data. Magn Reson Imaging 2005;23(1):75-81.
129. Wang Z. Improving cerebral blood flow quantification for arterial spin labeled perfusion MRI by removing residual motion artifacts and global signal fluctuations. Magn Reson Imaging 2012;30(10):1409-1415.
130. Wells JA, Thomas DL, King MD, Connelly A, Lythgoe MF, Calamante F. Reduction of Errors in ASL Cerebral Perfusion and Arterial Transit Time Maps Using Image De-Noising. Magn Reson Med 2010;64(3):715-724.
131. Murase K, Yamazaki Y, Shinohara M, Kawakami K, Kikuchi K, Miki H, Mochizuki T, Ikezoe J. An anisotropic diffusion method for denoising dynamic susceptibility contrast-enhanced magnetic resonance images. Physics in Medicine and Biology 2001;46(10):2713-2723.
132. Petersen ET, Lim T, Golay X. Model-free arterial spin labeling quantification approach for perfusion MRI. Magn Reson Med 2006;55(2):219-232.
133. Parkes LM, Tofts PS. Improved accuracy of human cerebral blood perfusion measurements using arterial spin labeling: Accounting for capillary water permeability. Magn Reson Med 2002;48(1):27-41.

134. Wang JJ, Alsop DC, Song HK, Maldjian JA, Tang K, Salvucci AE, Detre JA. Arterial transit time imaging with flow encoding arterial spin tagging (FEAST). Magnetic Resonance in Medicine 2003;50(3):599-607.
135. Wells JA, Lythgoe MF, Choy M, Gadian DG, Ordidge RJ, Thomas DL. Characterizing the origin of the arterial spin labelling signal in MRI using a multiecho acquisition approach. Journal of Cerebral Blood Flow and Metabolism 2009;29(11):1836-1845.
136. Zhou JY, Wilson DA, Ulatowski JA, Trajstman RJ, van Zijl PCM. Two-compartment exchange model for perfusion quantification using arterial spin tagging. Journal of Cerebral Blood Flow and Metabolism 2001;21(4):440-455.
137. Haida M, Yamamoto M, Matsumura H, Shinohara Y, Fukuzaki M. Intracellular and extracellular spaces of normal adult rat brain determined from the proton nuclear magnetic resonance relaxation times. J Cereb Blood Flow Metab 1987;7(5):552-556.
138. Matsumae M, Oi S, Watanabe H, Okamoto K, Suzuki Y, Sato K, Atsumi H, Goto T, Tsugane R. Distribution of intracellular and extracellular water molecules in developing rat's midbrain: comparison with fraction of multicomponent T(2) relaxation time and morphological findings from electron microscopic imaging. Childs Nerv Syst 2003;19(2):91-95.
139. Lascialfari A, Zucca I, Asdente M, Cimino M, Guerrini U, Paoletti R, Tremoli E, Lorusso V, Sironi L. Multiexponential T2-relaxation analysis in cerebrally damaged rats in the absence and presence of a gadolinium contrast agent. Magn Reson Med 2005;53(6):1326-1332.
140. Wells JA, Lythgoe MF, Choy M, Gadian DG, Ordidge RJ, Thomas DL. Characterizing the origin of the arterial spin labelling signal in MRI using a multiecho acquisition approach. J Cereb Blood Flow Metab 2009;29(11):1836-1845.
141. Gregori J, Schuff N, Kern R, Gunther M. T2-based arterial spin labeling measurements of blood to tissue water transfer in human brain. J Magn Reson Imaging 2013;37(2):332-342.
142. James F, Roos M. Minuit - System for Function Minimization and Analysis of Parameter Errors and Correlations. Computer Physics Communications 1975;10(6):343-367.
143. Wang JJ, Fernandez-Seara MA, Wang SM, St Lawrence KS. When perfusion meets diffusion: in vivo measurement of water permeability in human brain. Journal of Cerebral Blood Flow and Metabolism 2007;27(4):839-849.

144. Kim T, Kim SG. Quantification of cerebral arterial blood volume using arterial spin labeling with intravoxel incoherent motion-sensitive gradients. Magn Reson Med 2006;55(5):1047-1057.

145. Ewing JR, Cao Y, Fenstermacher J. Single-coil arterial spin-tagging for estimating cerebral blood flow as viewed from the capillary: relative contributions of intra- and extravascular signal. Magn Reson Med 2001;46(3):465-475.

146. Kelly ME, Blau CW, Kerskens CM. Bolus-tracking arterial spin labelling: theoretical and experimental results. Physics in Medicine and Biology 2009;54(5):1235-1251.

147. Kelly ME, Blau CW, Kerskens CM. Bolus-tracking arterial spin labelling: theoretical and experimental results. Phys Med Biol 2009;54(5):1235-1251.

148. Gregori J, Schuff N, Kern R, Gunther M. T2-based arterial spin labeling measurements of blood to tissue water transfer in human brain. J Magn Reson Imaging 2012.

149. St Lawrence KS, Frank JA, McLaughlin AC. Effect of restricted water exchange on cerebral blood flow values calculated with arterial spin tagging: a theoretical investigation. Magn Reson Med 2000;44(3):440-449.

150. Crone C. The Permeability of Capillaries in Various Organs as Determined by Use of the 'Indicator Diffusion' Method. Acta Physiol Scand 1963;58:292-305.

151. Cuenod CA, Balvay D. Perfusion and vascular permeability: basic concepts and measurement in DCE-CT and DCE-MRI. Diagn Interv Imaging 2013;94(12):1187-1204.

152. Simchon S, Jan KM, Chien S. Influence of reduced red cell deformability on regional blood flow. Am J Physiol 1987;253(4 Pt 2):H898-903.

153. Lenz C, Frietsch T, Futterer C, van Ackern K, Kuschinsky W, Waschke KF. Influence of blood viscosity on blood flow in the forebrain but not hindbrain after carotid occlusion in rats. J Cereb Blood Flow Metab 2000;20(6):947-955.

154. Dupire J, Socol M, Viallat A. Full dynamics of a red blood cell in shear flow. Proceedings of the National Academy of Sciences of the United States of America 2012;109(51):20808-20813.

155. Yeom E, Kang YJ, Lee SJ. Changes in velocity profile according to blood viscosity in a microchannel. Biomicrofluidics 2014;8(3):034110.

156. Cho YI, Mooney MP, Cho DJ. Hemorheological disorders in diabetes mellitus. J Diabetes Sci Technol 2008;2(6):1130-1138.

157. Banerjee R, Nageshwari K, Puniyani RR. The diagnostic relevance of red cell rigidity. Clin Hemorheol Microcirc 1998;19(1):21-24.
158. Calamante F, Gadian DG, Connelly A. Delay and dispersion effects in dynamic susceptibility contrast MRI: Simulations using singular value decomposition. Magn Reson Imaging 2000;44(3):466-473.
159. Kaur P, Singh G, Kaur P. A Review of Denoising Medical Images Using Machine Learning Approaches. Current Medical Imaging Reviews 2018;14(5):675-685.
160. Lipowsky HH, Sheikh NU, Katz DM. Intravital Microscopy of Capillary Hemodynamics in Sickle-Cell Disease. Journal of Clinical Investigation 1987;80(1):117-127.
161. Rodgers GP, Schechter AN, Noguchi CT, Klein HG, Nienhuis AW, Bonner RF. Periodic Microcirculatory Flow in Patients with Sickle-Cell Disease. New England Journal of Medicine 1984;311(24):1534-1538.
162. Wang M, Etu J, Joshi S. Enhanced disruption of the blood brain barrier by intracarotid mannitol injection during transient cerebral hypoperfusion in rabbits. Journal of Neurosurgical Anesthesiology 2007;19(4):249-256.
163. Chu PC, Chai WY, Hsieh HY, Wang JJ, Wey SP, Huang CY, Wei KC, Liu HL. Pharmacodynamic analysis of magnetic resonance imaging-monitored focused ultrasound-induced blood-brain barrier opening for drug delivery to brain tumors. Biomed Res Int 2013;2013:627496.

Printed by Media-Tryck, Lund 2018 NORDIC SWAN ECOLABEL 3041 0903

LUND UNIVERSITY
Faculty of Science
Department of Medical Radiation Physics
ISBN 978-91-7753-890-5